The Pennsylvania State University

The Graduate School

IN-SITU PROCESS MONITORING OF DIRECTED ENERGY DEPOSITION POWDER FLOW TO DETECT ANOMALIES

A Thesis in

Mechanical Engineering

by

Sheila Moroney

Submitted in Partial Fulfillment
of the Requirements
for the Degree of

Master of Science

May 2023

The thesis of Sheila Moroney was reviewed and approved by the following:

Edward Reutzel
Director of Center for Innovative Materials Processing Through Direct Digital Deposition Lab (CIMP-3D), Associate Research Professor, The Applied Research Laboratory, Mechanical Engineering
Thesis Advisor

Amrita Basak
Assistant Professor, Mechanical Engineering

Robert Kunz
Professor, Mechanical Engineering
Associate Head for Mechanical Engineering Graduate Programs

ABSTRACT

Directed energy deposition (DED) is a category of additive manufacturing (AM) that employs one of a variety of energy sources, (such as electron beam, laser, arc) to melt and deposit either powder or wire feedstock to build up standalone features or resurface existing components making DED a practical option for repair. Laser based directed energy deposition (LDED) additive manufacturing process is attractive for repair because of the ability to tailor process parameters to effectively restore part geometry while using the least amount of energy necessary to limit residual stress, distortion, and degradation of the base material. The use of LDED to repair parts in the aerospace and defense industries has helped to reduce costs of replacement parts. Currently, however, LDED lacks the reliability of other manufacturing processes. Many researchers have developed methods to monitor key process parameters of the LDED process in-situ. However, few studies have focused on a method to monitor the powder flow, a parameter that is critical to the success of a DED repair. And none have related variations in powder flow directly to deposition geometry and quality with data collected in-situ. The work presented in this thesis presents methods to monitor the powder flow rate and spatial powder flow distribution below the nozzle exit. In-situ powder flow monitoring analysis methods are developed and used to identify anomalies in the powder flow from nozzle exit through the powder focal plane. The ability for the system to detect a powder flow anomaly that impacts deposition quality is validated by performing a set of experiments that show the effect of irregular powder flow on build height.

TABLE OF CONTENTS

LIST OF FIGURES

LIST OF TABLES

ACKNOWLEDGEMENTS

This effort was funded under Rolls-Royce Corporation Research Agreement A19-0049 titled “Sensor-based Quality Monitoring of Directed Energy Deposition Additive Manufacturing.”

I would like to thank Scott Nelson and John Grubbs for their guidance and expertise throughout this project.

I would like to acknowledge Anil Chaudhary and Brandon Baucher from Applied Optimization for the use of their Anomaly Flagging System to monitor build quality in-situ. I am also very thankful for their insightful contributions over the course of this project.

I would like to thank all of the current and former employees of CIMP-3D ARL who have supported me, including, Peter Coutts and Tadd Meyer, but especially:

Cory Jamieson, for his endless patience, for teaching me how to use the LENS system, and for always helping out when it felt like everything was going wrong.

Jason Scherer, for sharing his great wealth of LabVIEW knowledge with me and being a continuous source of advice and encouragement.

Dr. Abdalla Nassar, for his extensive contributions in starting this project and for providing me the opportunity to work as graduate research assistant at ARL.

My advisor, Dr. Ted Reutzel, for his extraordinary expertise, for being a tremendous source of guidance and advice, and for helping me grow as an engineer.

I would like to express my immense love and gratitude for my parents, who are my biggest supporters, my greatest role models, and my best friends. Their guidance through every low and high, especially these last six years, has been invaluable. Look at us, who would’ve thought?

This thesis is dedicated to my brother Joe (and sister-in-law Julia), who inspired me to follow in his footsteps and pursue engineering at Penn State – and inadvertently do research involving lots of “calibrating”. And because he “weirdly” dedicated his master’s thesis to me.

Chapter 1

Introduction

Laser directed energy deposition (LDED) is a laser based additive manufacturing (AM) process that uses a focused laser beam to melt feedstock to form a deposition. One of the more common LDED processes is laser engineered net shaping (LENS, a trademark of Optomec) [1]. The process starts with a focused laser directed towards a substrate on an x-y stage. Powder is delivered to the substrate from a powder feeder and through a set of nozzles centered coaxially on the laser beam. The powder is heated by the laser and absorbed by the melt pool as the substrate moves with the stage, creating a solid clad or deposition. The deposition head, containing the powder nozzles and laser optics, increments in the z direction to start the next layer on top of the previous deposition. An example of a DED process is illustrated in Figure 1-1.

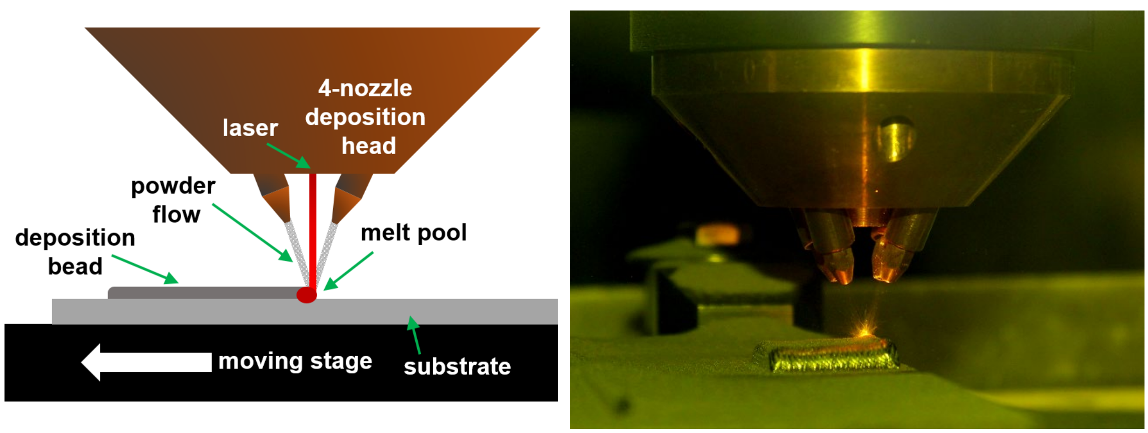

Figure **1-1**: Illustration and image of the DED process with a four-nozzle deposition head.

Directed energy deposition (DED) has become an increasingly common additive manufacturing process in the aerospace and defense industries for part repair [2]. Recently, additive manufacturing has shown the potential to greatly reduce the environmental impacts compared to traditional manufacturing processes [3], [4]. DED specifically has shown, through the repair of an automotive die, to significantly improve the impacts of mineral extraction, ecotoxicity, carcinogenics, and fossil fuels, when compared to a traditional welding repair counterpart [5]. For the improvement of environmental impacts across manufacturing industries to become more widespread, it is critical that the reliability of the DED process is improved.

Due to challenges in controlling the many parameters affecting the process, DED does not yet have sufficient reliability to run without fulltime observation by a skilled operator to look for errors. Studies investigating the various interactions between DED parameters to expand understanding of the process are widespread [6]. In powder-fed DED, powder flow is a parameter that is predisposed to anomalies, which can directly affect the build quality of the deposition [7]. Many research efforts have developed in-situ sensing methods to identify anomalies to help improve DED reliability [8]. In this work, a powder flow in-situ monitoring method is presented and powder flow analysis techniques and metrics are developed. The system and metrics are used in experiments that validate the anomaly detection capability of the monitoring method. Additionally, the system is used in combination with an in-situ build quality sensor that monitors the deposition surface, to relate the effect of powder flow anomalies directly to deposition quality. The implementation of in-situ sensing into industry is critical to improving the reliability and repeatability of the DED process and bringing DED to a broader range of industries.

The methods presented in this work focus on developing an automated in-situ powder flow monitoring (PFM) system to identify powder flow anomalies that occur at the nozzles. The PFM sensor comprises a laser line emitter and a high speed camera angled at the laser line. This sensor is able to collect cross section data of the powder flowing to the laser-material interactions, after the nozzle exit. The data can be used to construct the powder flow distribution which makes it easy to visually identify when a flow anomaly has occurred on a specific nozzle. The PFM sensor is mounted to a Z-stage providing the opportunity to record powder flow data through a range of locations below the nozzles to the focal plane of the powder stream, effectively capturing the spatial powder flow distribution in three dimensions. In addition, a calibration method was developed for the PFM sensor to estimate the mass flow rate of the powder. Implementing the PFM system on a DED machine could help to prevent build defects caused by powder flow anomalies before a build failure.

The literature review in chapter 2 surveys the current state of the art investigations of DED parameters, as well as methods for powder flow monitoring and identifying anomalies. In chapter 3, the methods for the DED system, the PFM sensor development, and the in-situ build quality monitoring system are presented. Chapter 4 discusses two experiments that aim to show the relationship between powder flow anomalies and build geometry by combining data from both the PFM sensor and the in-situ build quality sensor. Chapter 5 presents the results of the PFM calibration as well as the experimental results demonstrate the relationship between irregular powder flow and build geometry. In chapter 6, a summary is provided, conclusions of this effort are discussed, and potential future work is suggested.

Chapter 2

Literature Review

Process monitoring to assess and improve DED process reliability is broadly recognized as a being a critical step to widespread adoption in industry. To address this need, many researchers have developed methods for in-situ monitoring of various parameters of the DED process to improve reliability. Some of these methods include using a coaxial camera to monitor the melt pool [9]–[13] and optical emission spectroscopy to monitor melt pool vaporization [14]–[16]. Additionally, using a laser displacement sensor to measure the deposition height has been well established in literature [17]–[19]. Sammons et al. [17] developed a build sensing method that used a Keyence V7200 laser line scanner positioned perpendicular to the deposition path to scan the height of the build after each layer was completed. Chen et al. [18] used a similar displacement sensor with a clustering algorithm to detect and identify build surface defects based on the sensor's point cloud surface reconstruction. These similar methods using displacement sensors to monitor build height in-situ were very successful and have become common across DED process monitoring efforts. Despite the critical importance of powder flow rate for consistent deposition and build quality, in-situ monitoring of the powder flow rate near the powder focal plane has previously not been demonstrated.

Consistent layer height is necessary because incorrect deposited layer heights can lead to over or under building [20]. Powder flow rate has been found to directly affect the layer height and deposition quality. While neither over or under building is desirable, under building can be compensated for by repeating layers. However, over building would require an external process to remove material. Choi and Chang [20] performed an analysis of variance (ANOVA) to investigate the effect of a handful of process parameters on deposition height and quality. They found that the set powder flow rate had a significant effect on layer thickness [7]. Furthermore, Haley et al. [21] used a physics based, analytical model of powder flow and found a strong correlation between the location of working distance compared to the powder convergence distance or focal plane of powder. The powder capture efficiency was significantly lower when the melt pool was above and below the powder focal plane, resulting in a reduced deposited layer height. Moreover, Donadello et al. [22] used a coaxial imaging laser triangulation setup to monitor deposition height in-situ and found that powder capture efficiency is directly affected by the combination of laser power and powder flow rate.

Many processing parameters of the DED process contribute to powder flow behavior including the gas flow rates [23] and nozzle geometry [24]. Powder capture efficiency, i.e. the ratio of powder melted to powder fed, is often used as a metric to determine the quality of the powder flow [2]. DED processes employ several gas flows that can affect the powder flow. The carrier gas directly impacts the powder flow because it aids in transfer of the powder from the feeder to the deposition head [2]. In a DED process that is not contained in an inert atmosphere, a localized shielding gas flow must be used to prevent oxidation at the melt pool. This gas flow near the melt pool area could have a significant effect on powder flow [2]. Finally, the coaxial gas protects the laser optics, but is aimed near the powder flow. Typically argon is the gas used for the various gas flows, as well as the inert atmosphere in the processing chamber. Yao et al. [23] found that increasing carrier gas flow rate increased the velocity of the powder particles out of the nozzles. Particles with higher nozzle exit velocity have a shorter laser-particle interaction time. In addition, it has been found that a higher carrier gas flow rate increased the distance of the powder focal plane from the nozzles [24]. Takemura et al. [24] designed a coaxial nozzle that directed powder toward the laser center at a larger angle (to normal) than typical nozzles. They found that this designed nozzle decreased the distance of the powder focal plane from the nozzles, which improved powder capture efficiency at the melt pool.

Powder flow can be hindered by a variety of process anomalies, including clogs, material adhesion to nozzles, and fluctuations in flow rate from powder feeders. Powder that is oversized, or contains impurities, can lump together within the path from powder feeder to deposition head and cause a clog [25]. An example of an internal nozzle clog is shown in Figure 2-1. Powder adhesion to the nozzle occurs when powder ejects from the melt pool as hot spatter. As more hot spatter sticks to the nozzle, the nozzle increases in temperature [26]. With a hotter nozzle, the nozzle will continue to collect additional spatter, leading to a partial or complete blocking of the nozzle outlet and hindering powder flow as shown in Figure 2-1 [27]. In more extreme cases, the adhered spatter can grow large enough to block a portion of the laser beam [25]. In addition to these anomalies, powder feeders also contribute to powder flow irregularities [7], [28]–[30]. One study noted that the oscillating powder flow rate correlated with the hopper rotation speed [7]. A heavily used RPM wheel based powder feeder may cause the powder flow rate to oscillate up to 20% of the nominal flow rate [28].

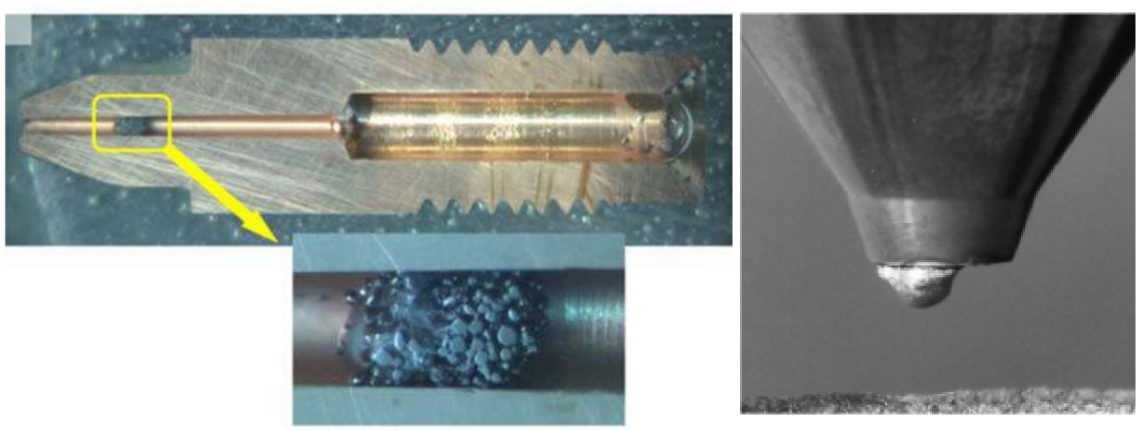

Figure **2-1**: Image of an internal nozzle clog (left) [6] and a chunk of powder adhesion to a coaxial nozzle (right) [2].

Many studies have developed models or simulations to predict powder flow behaviors. Computational fluid dynamics (CFD) simulations of the powder flow and gas flow have been developed to observe the effect of nozzle geometry [23], [24], and nozzle material [31] on flow rate. CFD has also been used to predict and describe the behavior and pattern of powder flow [23], [32]–[35]. Other simulation methods have been used to extract key insight into the DED process. For example, Monte Carlo simulations have been used to observe the gas flow and particle trajectories [36]–[39]. Additionally, Martinez-Marchese et al. used a Lagrangian simulation to track individual powder particles [40]. Physics-based analytical models have been developed to investigate powder particle behavior [21], [41], [42]. Liu et al. [41] created an analytical model to predict the powder distribution at various distances from the powder convergence. The powder flow was found to follow a Gaussian distribution at the focal plane and the individual powder flows at a distance above the focal plane.

Models of powder flow characteristics, have been experimentally validated using a variety of sensors. Several studies used a combination of a laser to illuminate the powder flow at the nozzle exit, and a camera placed at 90 degrees to capture the powder flow at the laser intersection [7], [24], [32], [35], [36]. Katinas et al. [35] used pulsed laser particle tracking velocimetry (PTV) to validate their CFD model of particle spray pattern. The pulsed laser was aimed at the vertical powder flow to capture two nozzles in plane and two out of plane. The digital camera, fitted with a macro lens, was aimed perpendicular to the laser plane and triggered by the pulsed laser. Using this method, Katinas et al. were able to analyze the velocity of individual powder particles. Other methods used to validate models include an optical camera [23], a high speed camera [33], and a weight measurement system [41]. While these methods of observing powder flow were successful in validating the simulations and models, they are not suitable for monitoring powder flow in-situ.

Because powder flow rate fluctuations can affect the build quality, it is critical that in-situ flow rate monitoring systems are developed. Hu & Kovacevic [10] developed a method to monitor powder flow rate as it exits the powder feeder. A laser diode emits a beam through the path of powder flow at a receiving photodiode. After a weight-based calibration, this system was able to measure the powder flow rate at 10 Hz and provided feedback control to the powder feeder to adjust the RPM setting of the rotational screw. Petrovic-Filipovic et al. [29] developed a powder flow rate monitoring method using flexible piezoelectric sensors. The sensors comprise ferroelectric polymers that detect localized pressure changes and convert that deformation to electric energy as a measurable voltage response. Similarly, Whiting et al. [30] used acoustic emission to monitor the mass flow rate of powder in-situ. The powder passes through a cylindrical channel on its path from the powder feeder to the deposition head. An acoustic emission sensor (piezoelectric transducer) is mounted to the cylindrical channel to measure the impacts of the particles. A calibration method was developed for the acoustic sensor to measure mass flow rate. The mass flow rate measured with the acoustic sensor was highly correlated to the mass flow rate measured by the scale. Although these methods were successful in monitoring the powder flow rate in-situ, they lack the capability to measure the flow rate after the powder has exited the nozzles. It is possible the powder flow rate could have significant variation further down the path to the deposition head due to powder flow anomalies at the nozzles. The powder flow rate characteristics after exiting the nozzles is a better representation of feedstock delivery the melt pool will receive, and is the critical location for observation.

Several additional methods to study powder flow monitoring have been developed. Using a high speed X-ray to image the interaction of powder entering the melt pool, Wolff et al. were able to determine the velocity of individual powder particles [43]. Alternatively, Reutzel et al. developed a method to create a 3D reconstruction image of powder flow from a four-nozzle system. They set up a filtered video camera perpendicular to a laser line scanner illuminating a vertical plane of the powder flow. The video frames were then used to construct a 3D representation of the powder in order to observe powder flow behavior including, the convergence angle from the nozzles and the size of the waist at convergence [44].

Few researchers have developed methods to identify anomalies from material adhesion on the powder nozzle. One method used a filtered camera to image the powder flow after the nozzle exit, reflecting from a perpendicularly placed laser line generator [45]. This method was able to detect a clogged nozzle, but was limited by the angle at which the camera viewed the nozzles. Conversely, Kelly [27] designed a nozzle embedded with thermocouples to detect a rise in temperature. A high temperature would indicate that a clog was present by accumulating powder sintering to the nozzle. Although this method worked well, it requires a custom modified nozzle, therefore, it is not easily adaptable for widespread DED processes. Kledwig et al. [26] used a coaxial CCD (charged-coupled device) camera and a dichroic mirror to detect and identify material adhering to the edge of a coaxial nozzle from radiation distribution. This experimental set up, paired with an algorithm, was able to detect most material nozzle adhesions. However, for some materials that emit higher electromagnetic radiation, the algorithm incorrectly detected the end of a melt pool as a nozzle adhesion. With a similar method, Lee et al. [25] developed a deep learning model that monitors the melt pool geometry with a coaxial camera to detect a variety of abnormal powder flow occurrences from a four-nozzle deposition head. The model was trained to detect changes in melt pool geometry from abnormal powder flow by intentionally clogging one nozzle at a time. This model was able to successfully detect powder flow anomalies in real time. However, the model was not trained to detect partially clogged nozzles. Additionally, this method requires a change in the melt pool geometry and cannot detect a powder flow anomaly out of process. Although these methods can contribute to identifying and detecting powder flow clogs, they lack the ability to detect fluctuations in the powder flow rate.

The methods for in-situ powder flow monitoring presented in this work are an advancement of the work done by Thomas [46]. The powder flow monitoring system has been modified for a four-nozzle deposition head and further developed with the addition of automation functionality for interlayer sensing. In-situ analysis, including automatic powder flow anomaly detection, was developed and incorporated into the system. Additionally, improvements to the PFM calibration method for estimating flow rate were implemented.

There has yet to be an in-situ powder flow monitoring system documented in current literature that has the capability to monitor powder flow distribution post nozzle exit, measure powder flow rate, and identify a specific nozzle flow anomaly. The effort in this work addresses these shortcomings by developing the methodology for a powder flow monitoring system and validating the anomaly detection capability through experiments that utilize a build quality sensor.

Chapter 3

Methods

The efforts in this work employed a powder-fed DED system with a vibratory based powder feeder to produce low flow rates. A powder flow monitoring system (PFM) was developed with the capability to estimate flow rate, collect powder distribution data after the nozzle exit, and detect powder flow anomalies. A calibration method was developed to obtain a conversion value to estimate powder flow rate. The PFM system used LabVIEW to run in-situ analysis that is able to detect powder flow anomalies during a build. In the experiments discussed in chapter 4, the PFM sensor was paired with a build quality sensor that measures build height in-situ to relate powder flow anomalies directly to build quality.

3.1 Directed Energy Deposition System

In this work the DED machine used for experiments was the Optomec LENS MR-7 with a 4-nozzle deposition head and a 500 W IPG Photonics Yb-doped fiber laser. The LENS system uses argon as the carrier gas, coaxial gas, and in the chamber to create an inert processing environment. The LENS has a 3-axis Galil Motion Control (DMC-18x2) stage system that is controlled by a custom program that receives DMC[1] files as tool path information. The main stage where the substrate is mounted, moves in the x and y directions, and the deposition head is mounted on the z stage. The feedstock used throughout this work was a fine Inconel 718 powder.

An Oerlikon 9MP Powder Feeder was used to deliver the powder to the deposition head. This powder feeder uses an air driven vibrator and carrier gas to create gas fluidization of the

[1] DMC files (.dmc) are tool path files specific for use with Galil DMC-Controllers. DMC code comprises two letter opcode commands that control the movement of the stage motors and laser. (https://www.galil.com/).

powder, as well as a closed-loop, weight-based control system to control the powder feed rate. This machine is able to remain relatively stable at the low flow rates that are used in this work.

3.2 Powder Flow Monitor Sensor Integration Development

To monitor the powder flow of a DED process in-situ, a sensor was positioned to collect data after the flow exits the nozzles. This sensor comprises a laser line and a camera angled toward the laser. For the remainder of this work, this sensor will be referred to as the PFM (powder flow monitoring) system or sensor. The PFM sensor is positioned with the laser line perpendicular to the direction of the powder flow and the camera positioned above it, directed down at an angle as show in Figure 3-1. With this orientation, the PFM sensor can collect data of the cross section distribution of the powder flow after the powder has exited the nozzles.

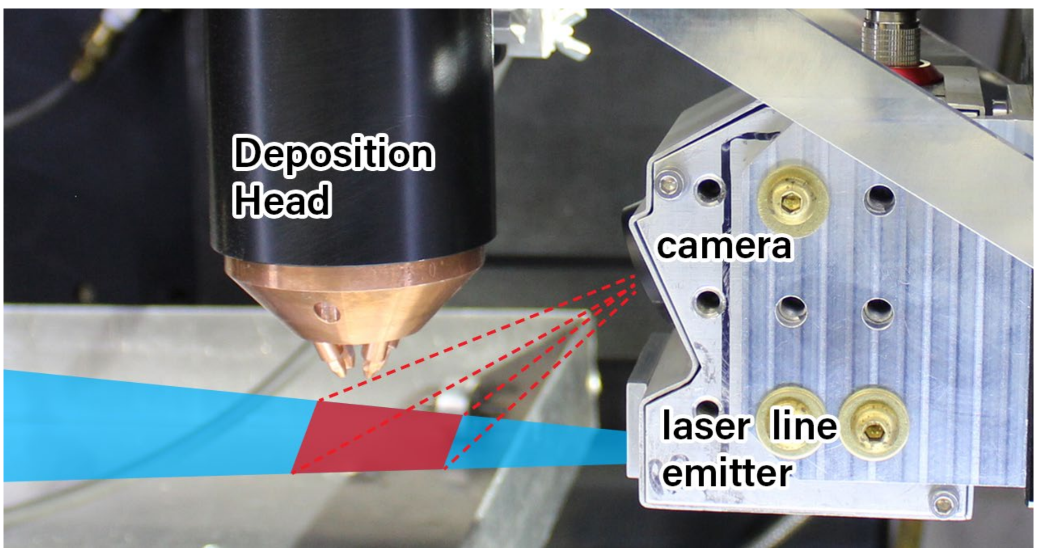

Figure **3-1**: Graphic of the range of the PFM sensor showing the camera sensor intersecting the laser line.

To monitor powder flow along the flow path, and to keep the PFM sensor out of the way during laser processing, the sensor was mounted on a vertical Z-stage as shown in Figure 3-2a. Both the PFM sensor and the Z-stage were controlled by a LabVIEW program. The Z-stage was automated to move in user-specified increments below the nozzles. This automation allows the PFM sensor to collect data at various points along the powder flow, including near the nozzle exit and at the working distance of the deposition head, where the powder converges as shown in Figure 3-2b. The LabVIEW program saved the data from the PFM sensor and the Z-stage to an SQLite database file (.db) used for post processing and in-situ powder flow analysis.

(a)

(b)

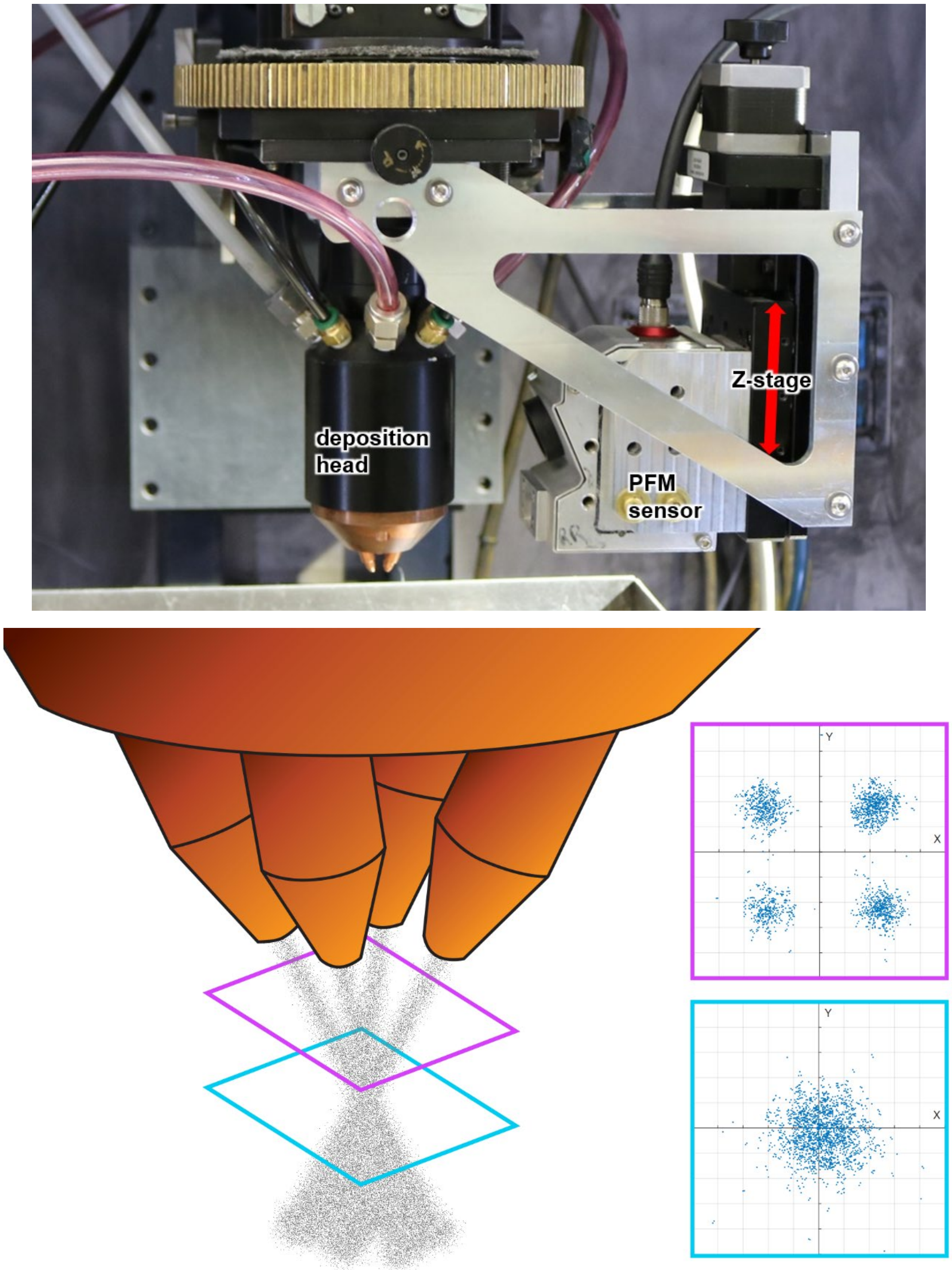

Figure **3-2**: (a) Image of the automation set up including the PFM sensor and the Z-stage. (b) A schematic showing the PFM powder distribution data at a z height near the nozzles and at the working distance.

The automated powder flow measurement starts at the end of each layer (or otherwise noted in the DMC code for the LENS). First, the deposition head moves up, out of the way of the substrate and the LENS control PC sends a trigger (using an NI-DAQ) to the LabVIEW program running on the PFM automation PC. The Z-stage moves the PFM sensor down to the user specified locations, recording the powder flow. When the PFM scans are complete, the stage moves back up and out of the way for laser processing to continue. The LENS control PC receives a trigger from the PFM automation PC to start processing the next layer. The schematic for the automation set up is shown in Figure 3-3.

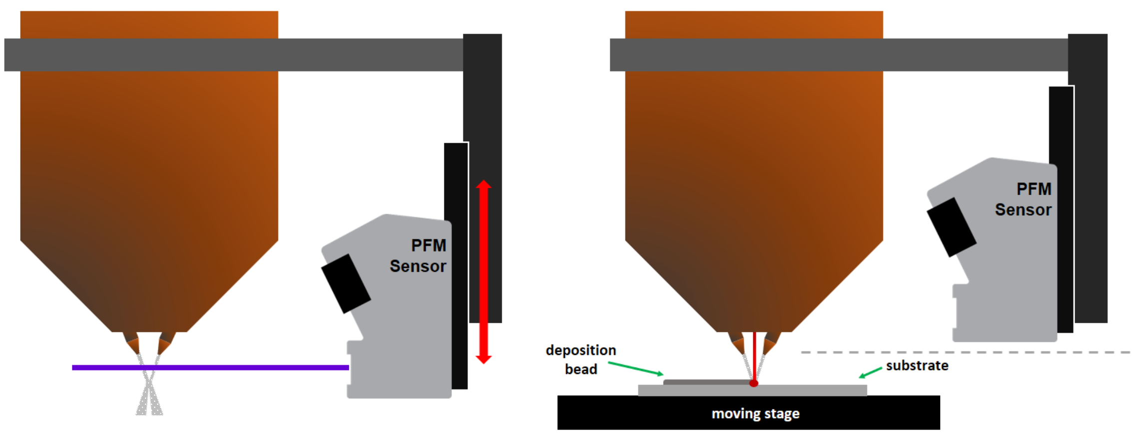

Figure **3-3**: A schematic of the set up for PFM automation. On the left, the PFM sensor is recording powder flow data at one Z height. On the right, the PFM sensor has moved out of the way for laser processing.

The PFM sensor[2] has a sample rate of approximately 1 kHz and an exposure time of approximately 100 µs. With these values, it can be calculated that the PFM sensor captures about 12% of the powder flow, as shown in Figure 3-4.

[2] The specific PFM setting values are proprietary information.

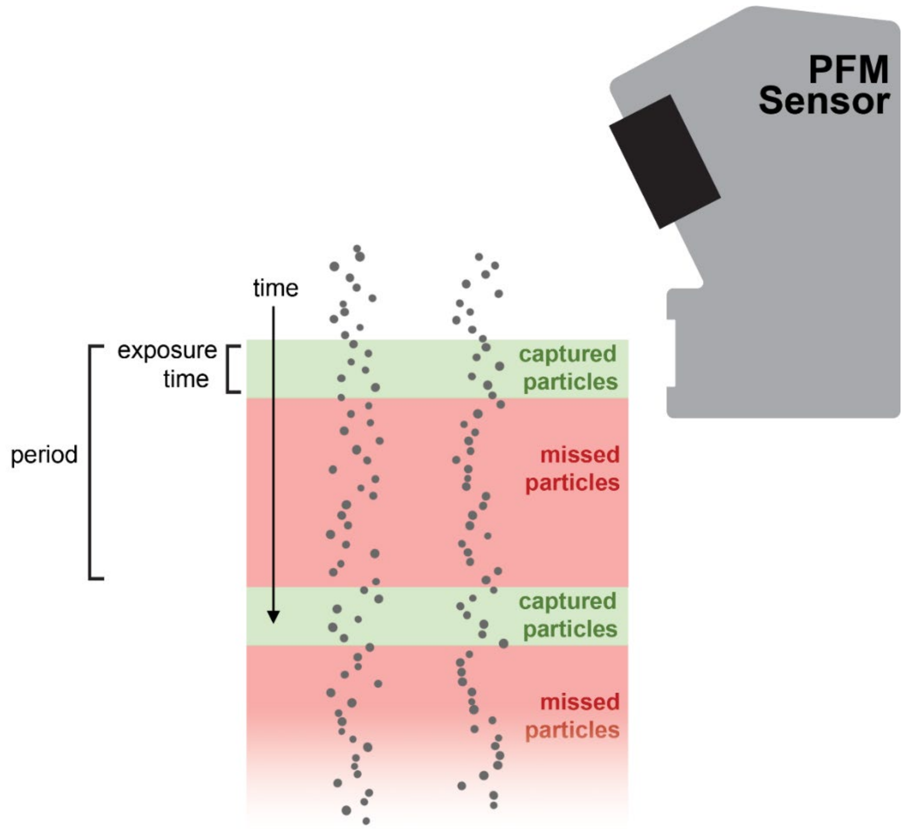

Figure **3-4**: A schematic of estimated percentage of powder captured by PFM sensor.

The PFM sensor records data points in X and Y coordinates. For the rest of this work, these data points will be referred to as *detections*. The PFM calibration method described in Section 3.2.1 calculates a conversion from detections over time to an estimated powder flow rate.

Due to the positioning of the PFM sensor and the angle of the camera within the sensor, there are restrictions on how close the sensor can get to the nozzles. If the sensor is too close to the nozzle exit, the two nozzles on the side of the sensor will block any data behind them as shown in Figure 3-5. When measuring powder flow at the closest distance to the nozzles (as opposed to nearer the powder focal plane), PFM can easily identify four distinct flows of powder in the cross section, which makes it the optimal height to detect an anomaly from a specific nozzle.

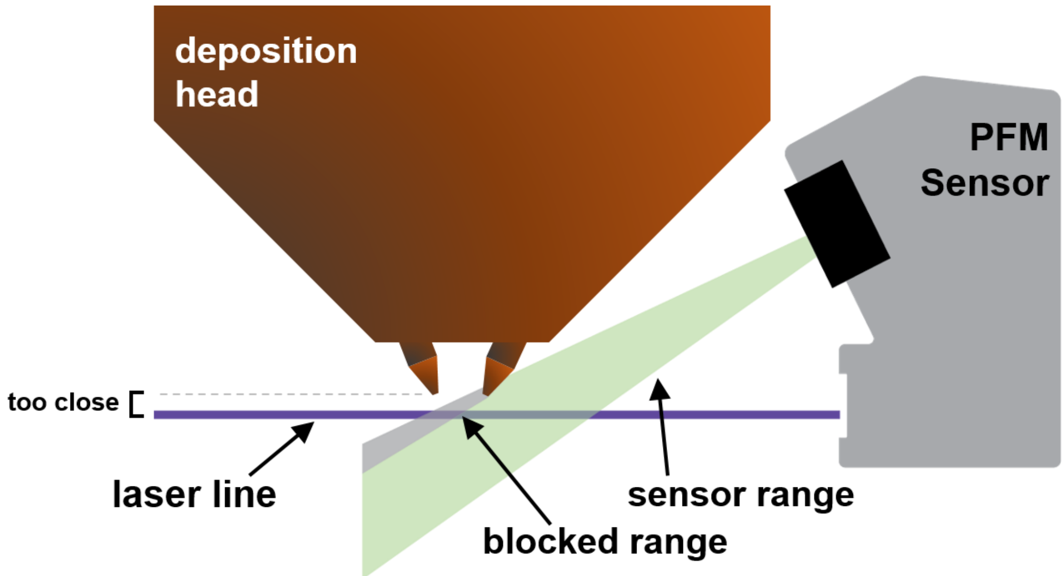

Figure **3-5**: An illustration of the effect of the nozzles shadowing any data behind them from the PFM sensor.

3.2.1 Powder Flow Monitoring Calibration

To monitor the powder flow rate, a calibration method was developed to relate PFM detections over time to a mass flow rate. The PFM sensor is synchronized with a scale that captures powder flowing out of the nozzles in real time, as shown in Figure 3-6. The scale used is a high precision balance from A&D Company with 0.001g repeatability and 0.002g linearity. When a calibration run starts, the PFM sensor and scale simultaneously collect data on the same powder flow. The scale is used to determine the actual flow rate of the powder. This scale is controlled by the same LabVIEW program that controls the PFM sensor. The data collected from the scale is added to the same database file as the PFM data for post processing. The scale has a sample frequency of approximately 10 Hz. To eliminate stray powder bouncing off of the scale, or back up into the range of the sensor, a unique container with a raised cone shape on the bottom was designed and 3D printed. The design objective was to ensure powder settles away from the center of the container, where both the coaxial gas and powder flow could disrupt the settled powder. Both the sensor and the powder collection container are placed as close as possible to the nozzles to ensure all powder is captured. The PFM sensor and scale collect data for 15 seconds for each test, across a range of powder flow rates.

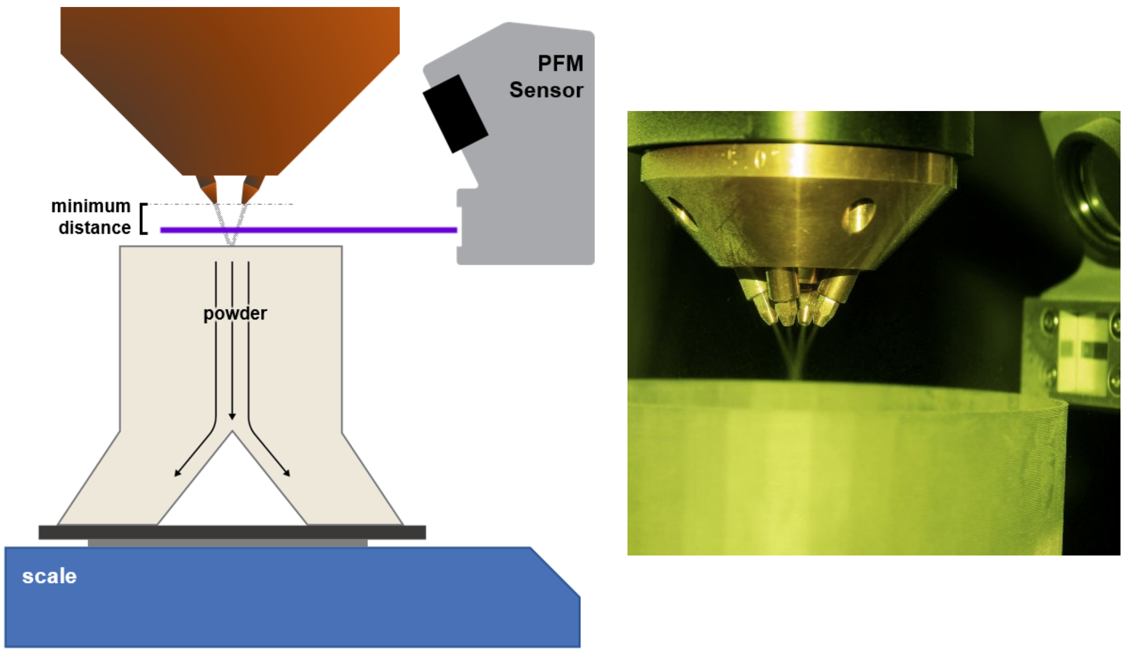

Figure **3-6**: Equipment set up for powder flow rate calibration (left) and image of powder flow during calibration (right).

The control system, including equipment used for both the PFM in-situ data collection and the PFM calibration, is summarized in Figure 3-7.

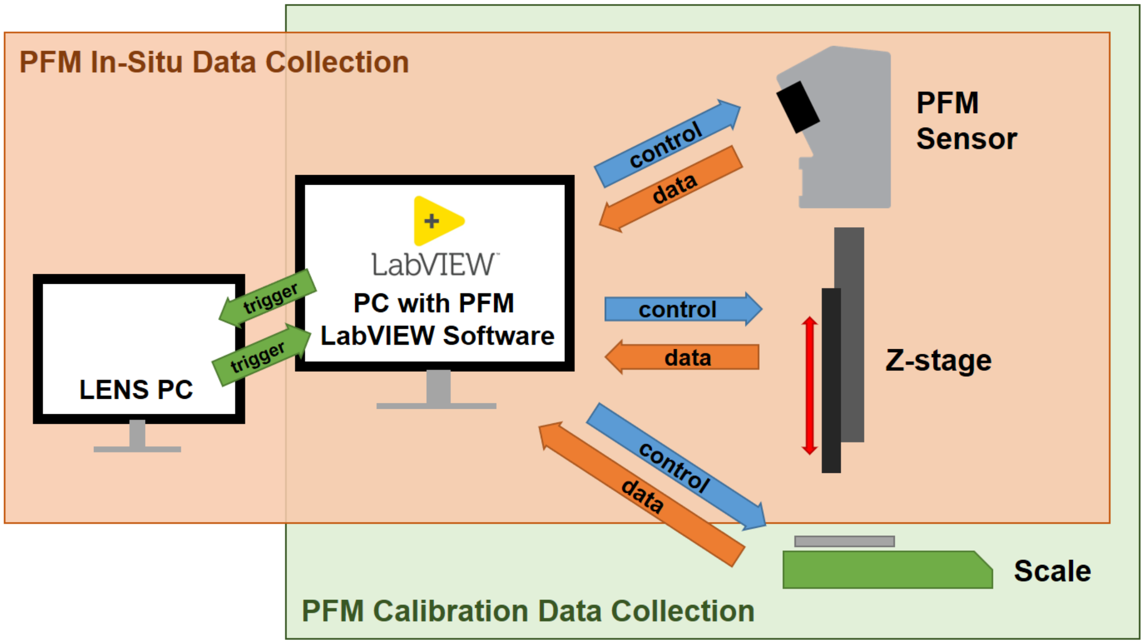

Figure **3-7**: Summary of information flow for each piece of equipment used in PFM in-situ analysis and calibration.

The scale records data in mass (grams) and time (seconds). The PFM sensor records data in number of detections and time (seconds). The actual flow rate (grams/sec) of the powder is determined from the slope of the scale data by plotting the mass vs. time. Then the PFM detection rate (detections/sec) is determined by obtaining the slope from plotting detections vs. time. To determine the conversion value, the flow rate from the scale is plotted with the PFM detection rate. The slope of this plot is the conversion value (detections/ gram) as shown in the Figure 3-8. This conversion value can then be used to determine the flow rate for any build using the same parameters.

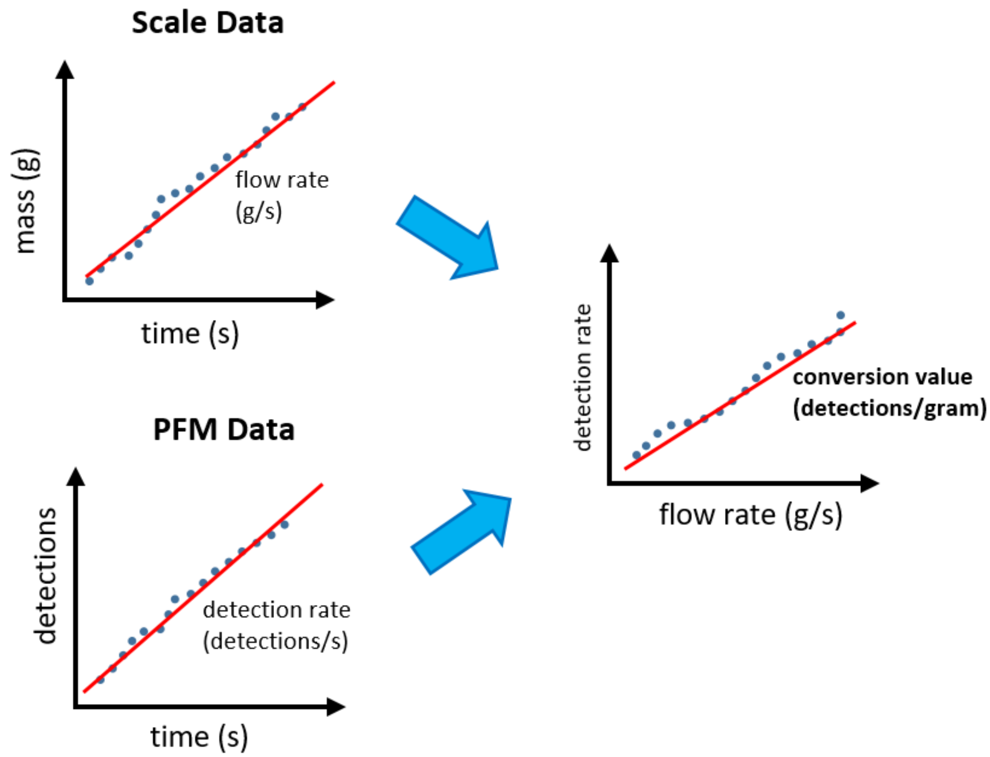

Figure **3-8**: Method for finding the calibration conversion value.

3.2.2 Powder Flow Monitoring In-Situ Analysis

The objective in developing in-situ analysis for the PFM sensor is to detect powder flow anomalies when they occur, so the build can be stopped before the anomaly affects the build quality. By using LabVIEW to process the data in-situ and a LabVIEW interface to display the data, a detected powder flow anomaly can be used to trigger an alert to the operator to pause the build. This monitoring method can help to prevent a powder flow anomaly going unnoticed and affecting the build quality. In this work, a flow anomaly refers to a partially or completely blocked nozzle, caused by an internal powder clog, or by material adhesion to the nozzles.

The PFM LabVIEW data analysis program imports the database file containing the PFM powder collection detection data as soon as the automated data collection has been completed.

The PFM data is split into sections determined by the individual z height of each scan. The default z height that is displayed to the operator on the software interface is the first scan below the nozzles exit. However, LabVIEW performs the same analysis at all z heights, and the user can change which z height is displayed. The same analysis is performed at the working distance of the deposition head, where the powder flow is expected to converge.

The estimated flow rate is determined by plotting the detections for a single z height scan over time. The slope of this data is multiplied by the conversion value that was determined during the PFM Calibration and divided by 60 seconds to provide the estimated flow rate in grams per minute.

For each nozzle, the two metrics used to determine if there is a flow anomaly are the width of the flow and the density of the flow. At an individual z height, the data is plotted on an x-y scatter plot to view the cross section of the powder flow. The x and y locations of the data are adjusted by the user so that the powder flow from each of the 4 nozzles resides in its own quadrant. Each flow is analyzed individually by plotting the data to a histogram in both x and y directions. Then the histograms are fit using Gaussian curves as shown in Figure 3-9.

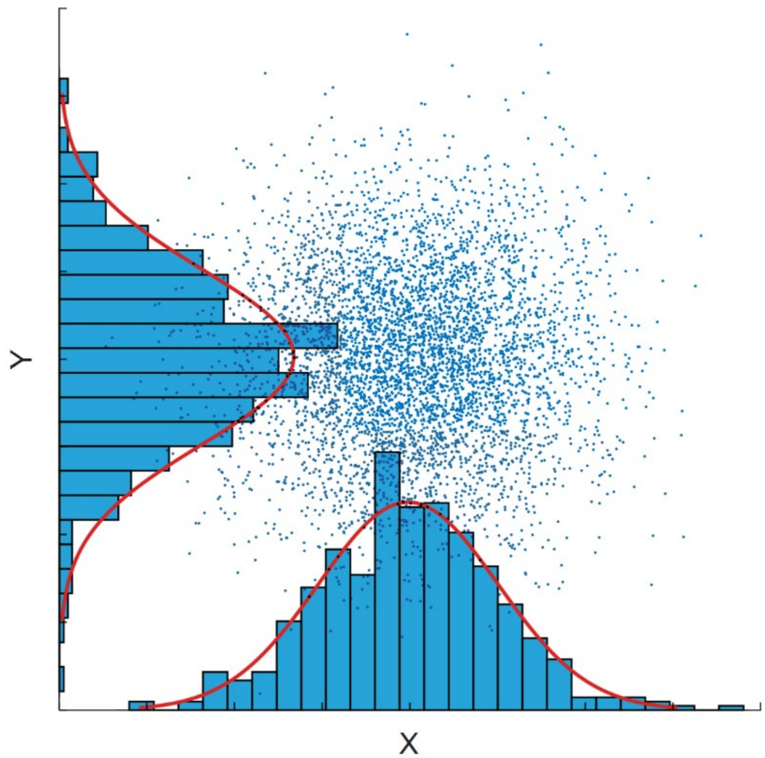

Figure **3-9**: An illustration of the X and Y direction histograms and Gaussian fits derived from one nozzle powder cross section.

The flow width is determined by using two standard deviations from the mean of the Gaussian fit. This selection of data captures approximately 95% of the powder flow per nozzle, removing any stray or outlier detections. The relative flow density of each flow is determined by dividing the number of particles in a quadrant by the total number of particles in the single cross section scan. During processing, the PFM measurements are captured after each layer is processed. The flow width values from each of the four nozzles are plotted as a function of layer to reveal any trends that may occur throughout a build. A similar plot is created for the relative flow densities for each nozzle. These plots have user specified ranges for acceptable values. When a width or density is outside the range, an alert is displayed on the user interface indicating that a flow anomaly has occurred. An example of a flow width plot and a relative flow density plot showing an anomaly are shown in Figure 3-10. A similar analysis is performed with the PFM sensor at the working distance, where the four separate flows have converged into one. Gaussian fits of the x and y histograms determine the width and density of the powder flow at the working distance. The user has the option to toggle the working distance data to be visible on the same chart.

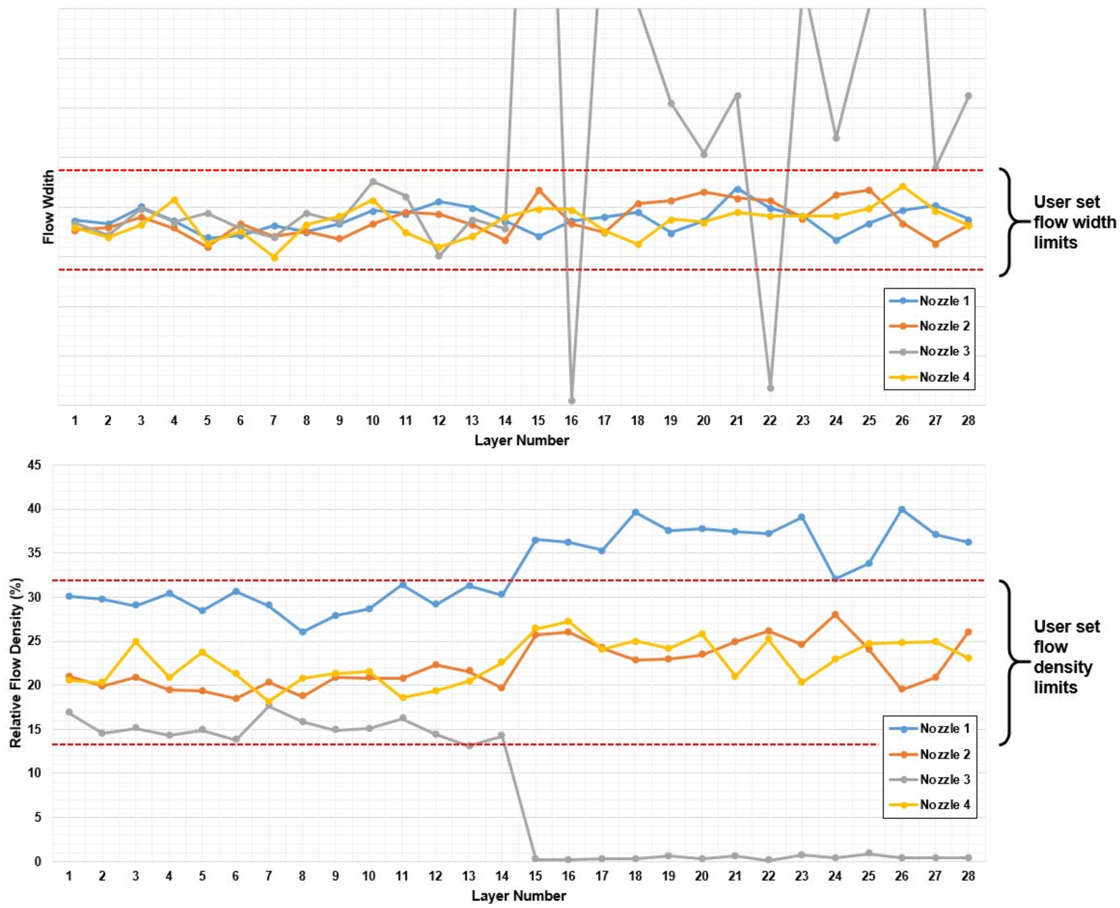

Figure **3-10**: An example of a flow width plot and relative flow density plot showing how the PFM LabVIEW program can detect an anomaly for a specific nozzle based on the user set limits.

3.3 Build Quality Sensor

The in-situ build quality sensing system used in this work was developed by Applied Optimization (https://appliedo.com/). This system will be referred to as the Anomaly Flagging System (AFS). The AFS sensor is a laser line scanner that collects surface data of the deposition in-situ. An external AFS control PC is connected to the LENS control PC as well as the AFS sensor. The AFS sensor is mounted to the z-axis of the LENS behind the deposition head, angled down, with the center of its range aimed a few millimeters behind the laser-substrate interaction zone as shown in Figure 3-11.

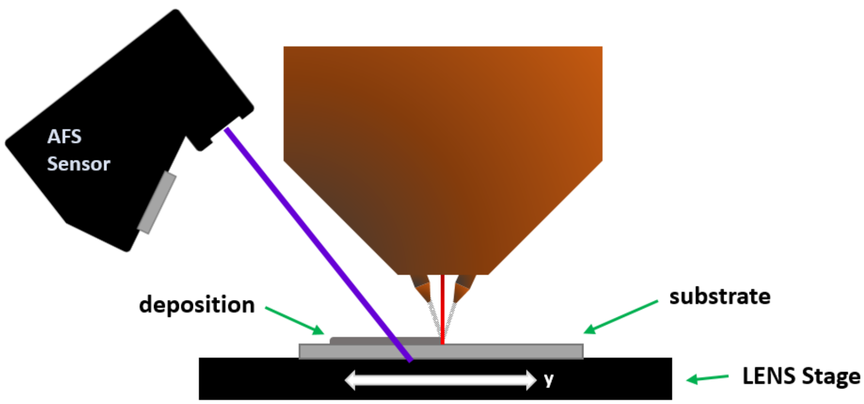

Figure **3-11**: Illustration of AFS Sensor physical set up during laser processing.

When the laser is on, the LENS control PC triggers the AFS to begin collecting data. The sensor captures the surface topology of the build as each track is deposited, either measuring ahead or behind the laser, depending on the direction the stage moves. The data is exported as a 2D array of z heights, to be processed in MATLAB.

Chapter 4

Experiments

Experiments were developed to determine if powder blockage anomalies that occur during processing result in build defects by synthesizing PFM powder flow data with AFS build surface data.

As discussed in Chapter 2, powder flow anomalies that occur for a variety of reasons during DED processes can lead to partial or full blockage of powder nozzles. For example, a powder clog within the nozzle can result in a full nozzle blockage. This was observed in a prior experiment using the same DED system, deposition head, and powder, in which a nozzle clog occurred as a result of poorly sieved powder. The PFM data showing the cross section of the powder flow from this experiment, which can be seen in Figure 4-1, clearly illustrates the impact this clog had on the resulting powder flow.

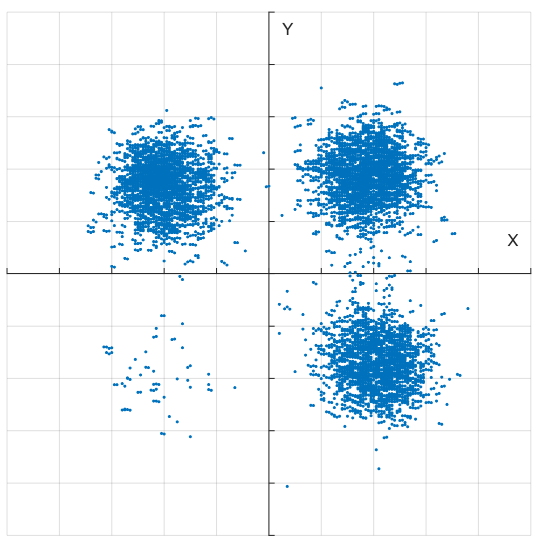

Figure **4-1**: PFM powder flow data collected at a z-height above the powder focal plane during a single naturally occurring nozzle clog on a four-nozzle DED system. Each block represents 1 mm.

Excessive nozzle heating during processing is another phenomenon that can lead to nozzle blockage. As the DED process runs, heat buildup and condensate affect the surface of the powder flow nozzles such that powder or spatter from the melt pool can more easily adhere to the nozzles. As more powder adheres, the resulting material build up can eventually block the powder flow from a nozzle. This effect was observed in an experiment involving Inconel 718 DED processing with a high flow rate. In this case, the material adhesion effect occurred organically, and resulted in partial blockage of one of the nozzles, as shown in Figure 4-2a. PFM captured cross section data of the powder flow, after the blockage had formed, shown in Figure 4-2b.

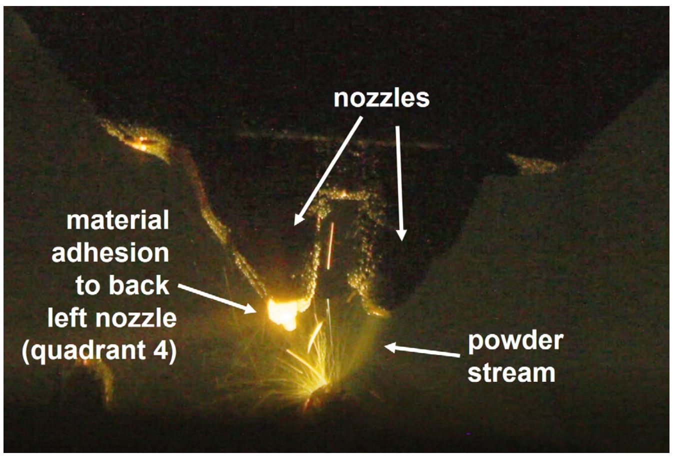

(a)

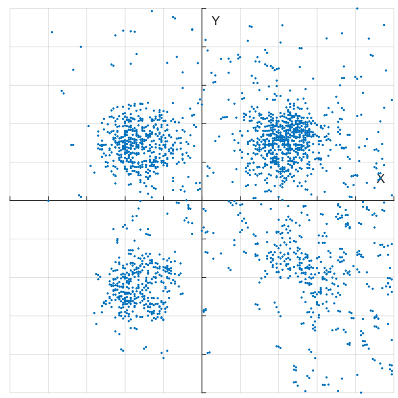

(b)

Figure **4-2**: (a) Image of the same material build up on nozzle, glowing after hot powder spatters into it from melt pool. (b) PFM powder flow distribution collected at a z height above the focal plane during partial blockage caused by material adhesion to a nozzle. Each block represents 1 mm.

4.1 Forced Anomaly Experiment – Full Blockage of One Nozzle

To assess the impact of nozzle blockage in a systematic way, a series of controlled experiments were designed. The purpose of this experiment is to compare the build quality that results from a series of nominal builds to builds with a forced anomaly. One nozzle will be intentionally fully blocked to represent a nozzle clog. The nominal builds will be compared to the anomalous builds through in-situ monitoring of powder flow and build geometry.

This experiment was conducted on an Optomec LENS MR7 in a fully inert argon environment. The depositions were created using an Inconel powder and nickel substrates. The majority of essential processing parameters (coaxial gas flow rate, laser spot size, laser power, travel speed, layer height, and hatch width) were derived from internal parameter development and remained consistent throughout the experiment. The powder flow rate was set to match the low flow rates that are common in the aerospace industry to repair high precision parts.[3]

The experiment consisted of four different build geometries: single bead, thin wall, pad, and air foil. The single bead was a one track deposit 76.2 mm (3 in) long. The thin wall was one track wide, 63.5 mm (2.5 in) long, and 20 layers (corresponding to roughly 0.25 in) tall. The pad was a rectangular geometry 10 tracks (corresponding to roughly 0.2 in) wide, 76.2 mm (3 in) long and 30 layers (corresponding to roughly 0.4 in) tall. The air foil build was a representative air foil geometry, repeated for 30 layers (corresponding to roughly 0.4 in). Each build type was deposited twice for a total of eight builds. The experimental build plan is displayed in Table 4-1. The relative build layout is shown in Figure 4-3. The first build of each type was processed with nominal powder flow. The second build of each type was the "anomaly" build. The first half of the build was processed with nominal powder flow. Then the build was paused and the front left nozzle was swapped with a fully blocked nozzle. The build was then resumed without any other deviations from nominal conditions. For example, the second thin wall build was paused after layer 15 was completed. The nozzle swap happened, and the remaining 15 layers were deposited with the powder flow blockage.

[3] The specific processing parameter values are proprietary information.

Table **4-1**: Full blockage anomaly experimental build plan.

Fig 4-3	Build Type	Tracks	Layers	Length	Powder Flow
a	Single Bead	1	1	76.2 mm (3 in)	Nominal
a	Single Bead	1	1	76.2 mm (3 in)	Anomaly
b	Thin Wall	1	30	63.5 mm (2.5 in)	Nominal
b	Thin Wall	1	30	63.5 mm (2.5 in)	Anomaly
c	Pad	10	20	76.2 mm (3 in)	Nominal
c	Pad	10	20	76.2 mm (3 in)	Anomaly
d	Airfoil	-	20	-	Nominal
d	Airfoil	-	20	-	Anomaly

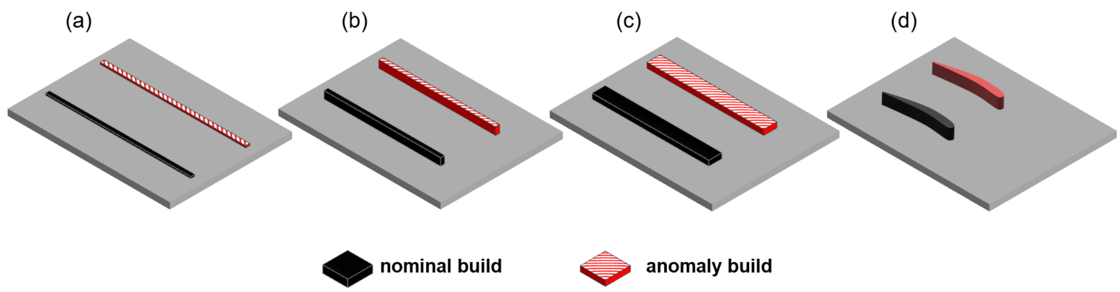

Figure **4-3**: Build plans for each build type. The nominal build is black and the manual anomaly build is red. (a) single beads, (b) thin walls, (c) pads, (d) air foils.

The intentional nozzle blockage anomaly was created by placing a piece of metal solder inside the nozzle as shown in Figure 4-4. This blockage represents the effect of an internal powder clog.

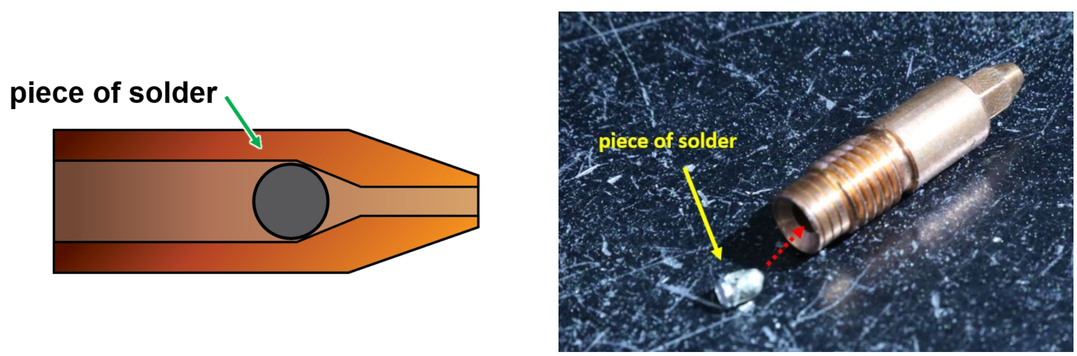

Figure **4-4**: An illustration of the forced nozzle anomaly. A piece of solder was placed inside the one nozzle halfway through each anomaly build. The nozzle is ~19 mm (0.75 inch) long.

To confirm that the solder-blockage represented the effect of an actual nozzle clog, a quick test was run. The PFM sensor took a scan below the nozzles, at nominal powder flow rate. The test was successful in creating a similar blockage effect to a real clog as seen in Figure 4-5.

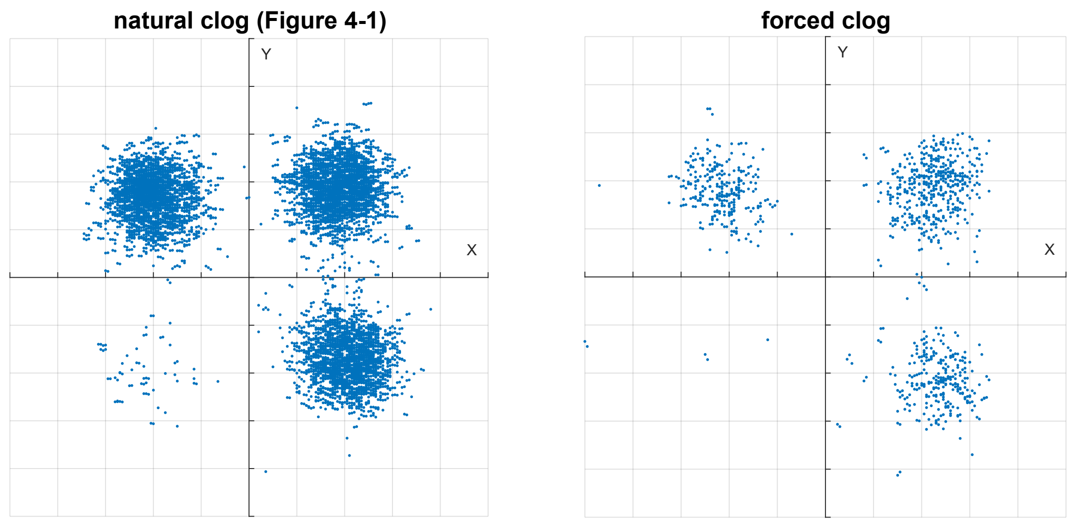

Figure **4-5**: PFM powder flow data test of forced nozzle anomaly using solder to create a clog on nozzle three compared with a natural clog. Each block represents 1 mm.

4.2 Forced Anomaly Experiment – Partial Blockage of One Nozzle

The purpose of this experiment is to compare a series of nominal builds to builds with a partially blocked nozzle to represent material adhesion to a nozzle tip that naturally occurs from time-to-time during DED processing. The quality of the nominal builds will be assessed and compared to the anomalous builds through in-situ monitoring of powder flow and build geometry.

The experiment consisted of three different build geometries: thin wall, pad, and air foil. The thin wall was one track wide, 63.5 mm (2.5 in) long, and 20 layers (corresponding to roughly 0.25 in) tall. The pad was a rectangular geometry 10 tracks (corresponding to roughly 0.2 in) wide, 76.2 mm (3 in) long and 30 layers (corresponding to roughly 0.4 in) tall. The air foil build was a representative air foil geometry, repeated for 30 layers (corresponding to roughly 0.4 in).

Each of these builds were deposited twice for a total of six builds. A summary of the build plan is displayed in Table 4-2. The first build was at nominal conditions. . At the halfway point of the second build, one nozzle was partially blocked to represent the effect of material adhesion interfering with powder flow. The relative build layout is show in Figure 4-6.

Table **4-2**: Partial blockage anomaly experimental build plan.

Fig 4-3	Build Type	Tracks	Layers	Length	Powder Flow
a	Thin Wall	1	30	63.5 mm (2.5 in)	Nominal
a	Thin Wall	1	30	63.5 mm (2.5 in)	Anomaly
b	Pad	10	20	76.2 mm (3 in)	Nominal
b	Pad	10	20	76.2 mm (3 in)	Anomaly
c	Airfoil	-	20	-	Nominal
c	Airfoil	-	20	-	Anomaly

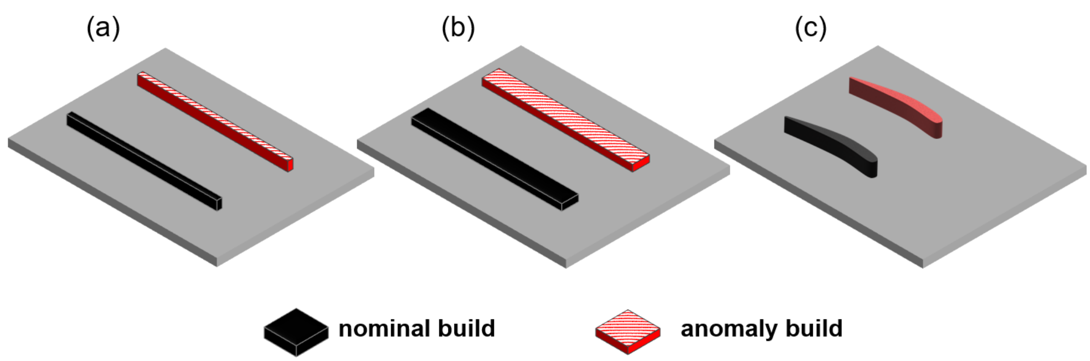

Figure **4-6**: Build plans for each build type. The nominal build is black and the manual anomaly build is outlined in red. (a) Thin walls, (b) pads, (c) air foils.

To achieve a partial nozzle blockage, a 2D stage was mounted to the deposition head. A thin metal plate was attached horizontally to the stage as shown in Figure 4-7. During the nominal builds, the plate was moved out of the way and did not interfere with the powder flow. For the anomalous builds, the build was paused after half the layers had been deposited. The operator used the stage knobs to position the metal plate to block a portion of the far left nozzle. To confirm that the metal plate was in the correct position, the PFM sensor collected powder flow data during a test scan. As shown in Figure 4-8, the powder flow data matches the effect of the naturally occurring material adhesion shown in Figure 4-2b.

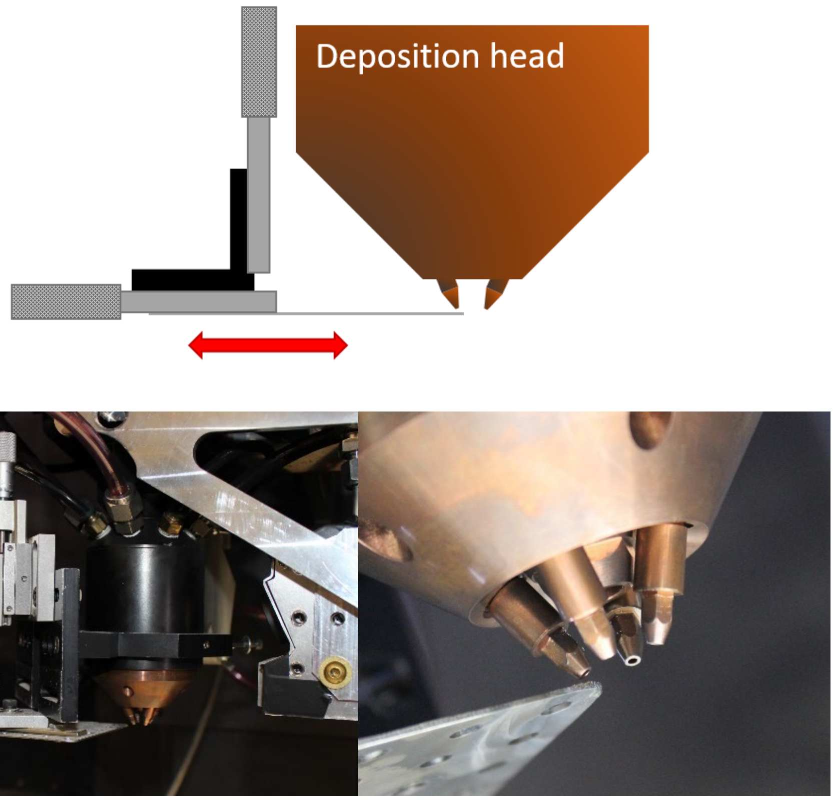

Figure **4-7**: Illustration and images of experimental set up to create a partial blockage of one nozzle.

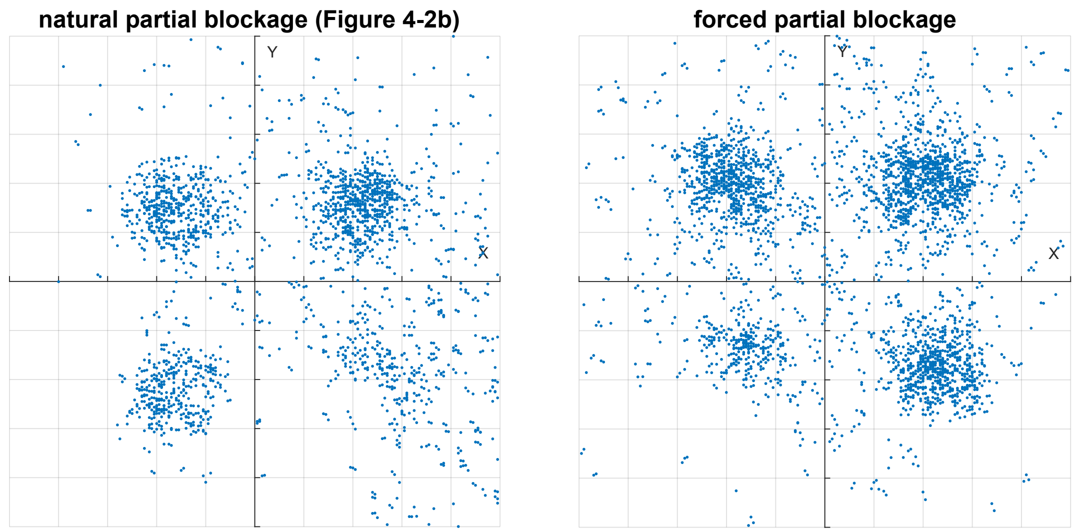

Figure **4-8**: PFM powder distribution with forced partial blockage in place compared with natural partial blockage. Each block represents 1 mm. Close up image of the metal plate partially blocking nozzle three.

4.3 Data Collection and Analysis

4.3.1 In-Situ Data Collection

Both experiments used the custom PFM powder flow collection system for in-situ data collection and analysis. For each build, the PFM system performed a set of automated scans after each layer was completed. The scans ranged from below the nozzle exit to the powder focal plane in half millimeter increments, for a total of 10 scans. One set of automated scans took about 40 seconds to complete. The in-situ data was processed through LabVIEW, and as previously stated, the results were displayed on a monitor, as each layer was completed. The calibration value determined from the PFM calibration was used to determine and display the estimated flow rate. The AFS sensor recorded surface topology data for each individual track. For the airfoil build, AFS was recorded for just a single scan over the build at the end of each layer with the laser off.

4.3.2 Post Process Analysis

The AFS data were processed to compare the build geometry of the nominal builds to the anomaly builds. The single bead substrate was cross sectioned for further analysis. The plate was cross sectioned in three places; at the beginning of the track, in the middle, and at the end. Each cross section was polished, etched and then imaged for a comparison.

Chapter 5

Results and Discussion

5.1 Calibration Results

Prior to experiments, the PFM system was calibrated to determine the powder flow rate conversion value needed for the specific combination of powder, gas flow rate, and deposition head. The calibration consisted of 20 fifteen second scans at a range of set flow rates near the nominal flow rate used in the experiments. For each scan the actual mass flow rate of the powder was determined from the scale data, and the powder detection rate was determined from the PFM data. These two values were plotted against each other as shown in Figure 5-1. Using a linear regression, the data shows a strong linear correlation with an R-squared value of 0.9784. Additionally, the 95% confidence intervals were calculated to show the range of the expected linear regression. The 95% prediction intervals were calculated to show the expected range of a new sample. The slope and offset value of the regression line were used as the conversion value to estimate flow rate during the experiments.

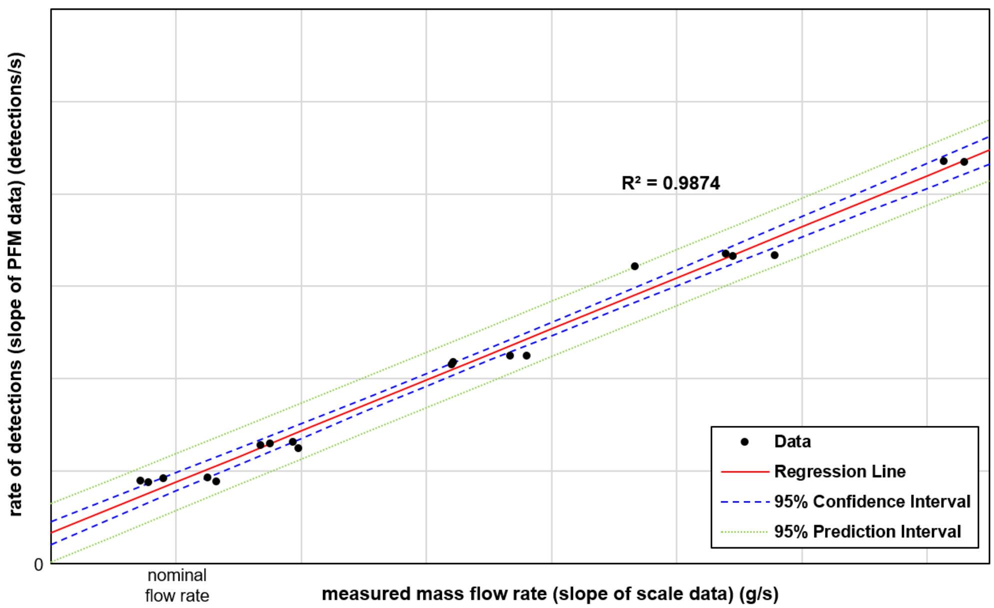

Figure **5-1**: Plot of detection rate (PFM slope) vs mass flow rate (scale slope) with a regression line and confidence and prediction intervals.

5.2 Full Nozzle Blockage Anomaly Experiment Results

Images of depositions from the first experiment are shown in Figure 5-2. For ease, some builds were constructed on the same substrate. The substrate was not let to cool in between builds.

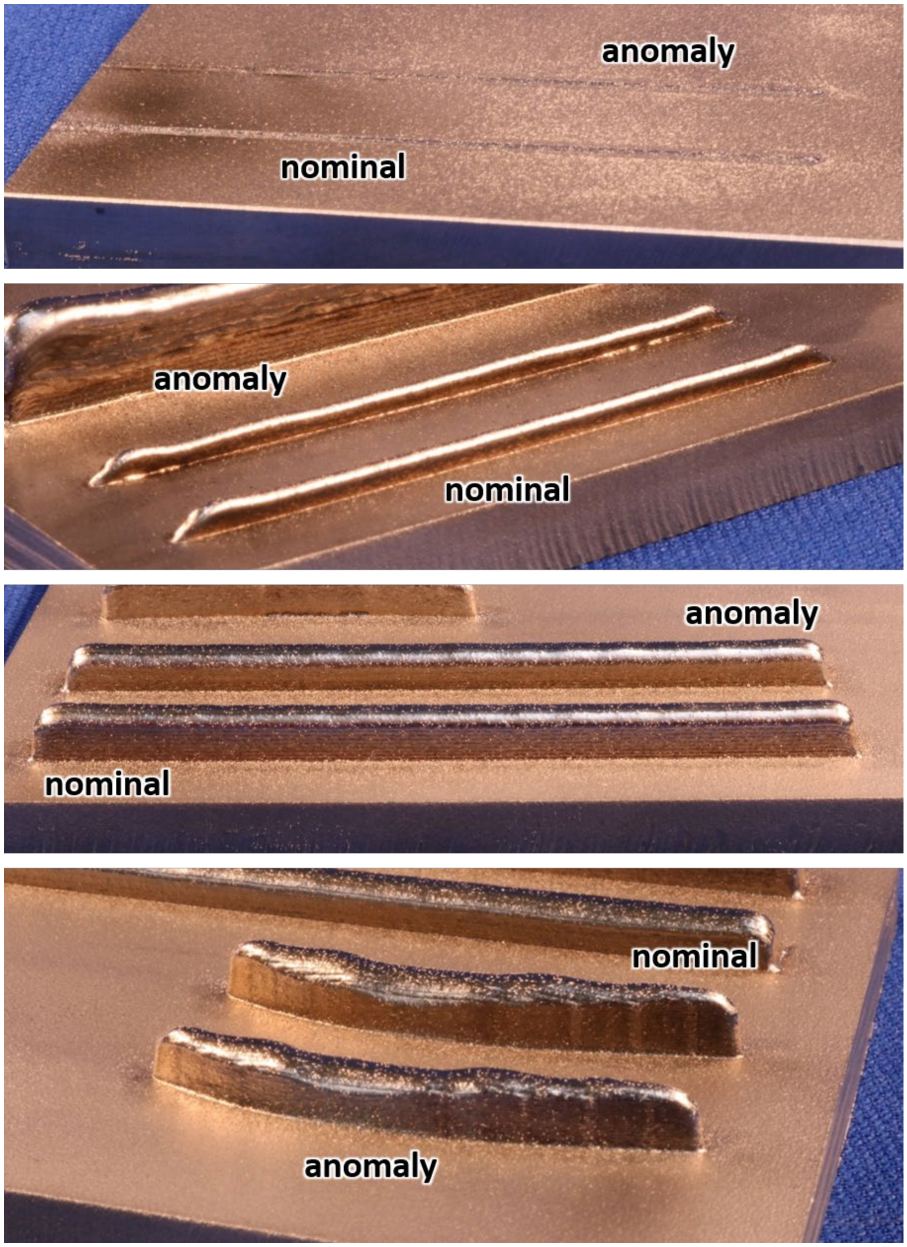

Figure **5-2**: Images of completed builds from the full nozzle blockage experiment. From top to bottom: single beads, thin walls, pads, airfoils.

The AFS data was analyzed and filtered in MATLAB. The data contained high z values scattered throughout, indicating the sensor captured stray powder particles. These values were filtered out using the *filloutliers* function in MATLAB. The *filloutliers* function located outliers as a point outside a number of standard deviations from a moving mean or by a percentile based threshold. The function replaced the outlier values with a nearest neighbor or a linear method [47]. Some values were so high, they were out of range of the sensor and recorded as NaN (Not a Number) values. These values were replaced using the *fillmisssing* function in MATLAB. The *fillmisssing* function replaced the missing values with a nearest neighbor or a linear method [47]. An example of the data from the nominal airfoil build, showing the filtered and post-process data, is shown in Figure 5-3.

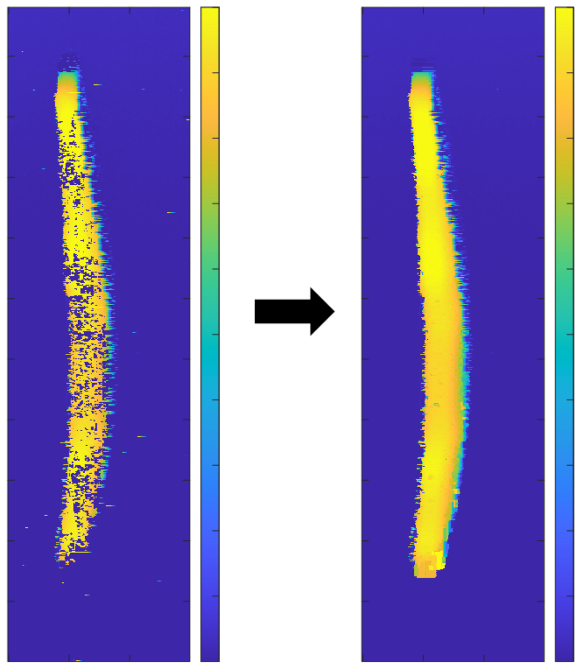

Figure **5-3**: Surface plot before (left) and after (right) filtering of the raw AFS data. Nominal Airfoil build from the full nozzle blockage experiment.

The cross section data of the powder flow from the PFM sensor before and after the intentional nozzle clog anomaly is shown in Figure 5-4. The nozzle clog was implemented in the third quadrant and completely blocks the powder flow from that nozzle. The working distance, where the powder converges and meets the melt pool, also shows a reduction of powder in the third quadrant, no longer retaining the circular shape seen in the nominal flow. The powder distribution at the working distance also appears less dense than the nominal flow. This distribution data remained consistent for each build in this experiment.

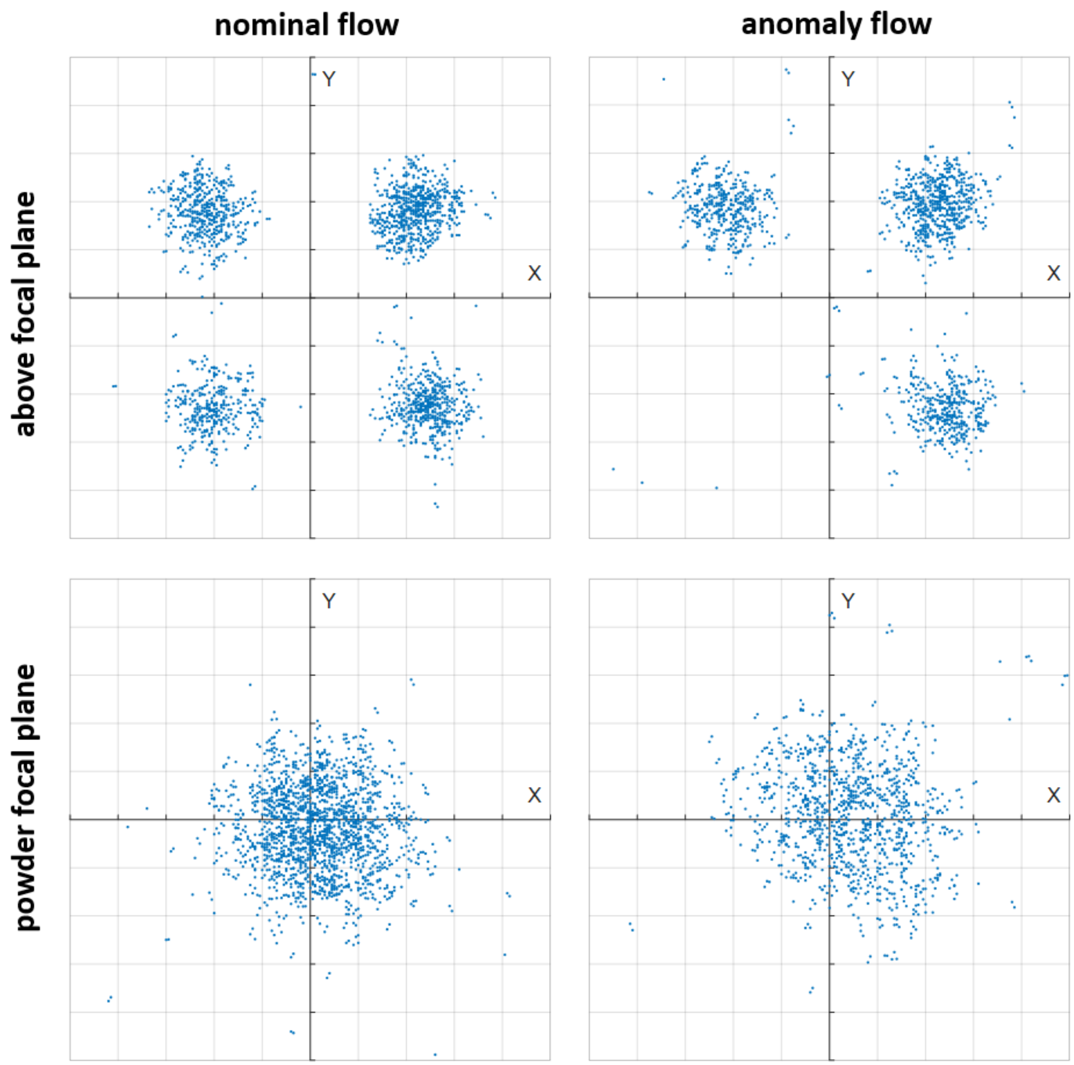

Figure **5-4**: Powder cross section distribution with nominal flow and with one nozzle blocked above the focal plane and at the focal plane. Each block represents 1 mm.

5.2.1 Single Beads

Images of the single bead depositions and the build height data from the AFS sensor are shown in Figure 5-5. The build height data does not show an obvious difference between the nominal single bead and the anomaly single bead. The build height surface plots also show that the substrate was not level or flat. The height of both the substrate and deposition at the beginning of the track is much higher than the end of the track. Since subsequent analysis of these builds were performed at cross sections of the deposition in the x direction, the change in substrate data in the y direction did not affect the results.

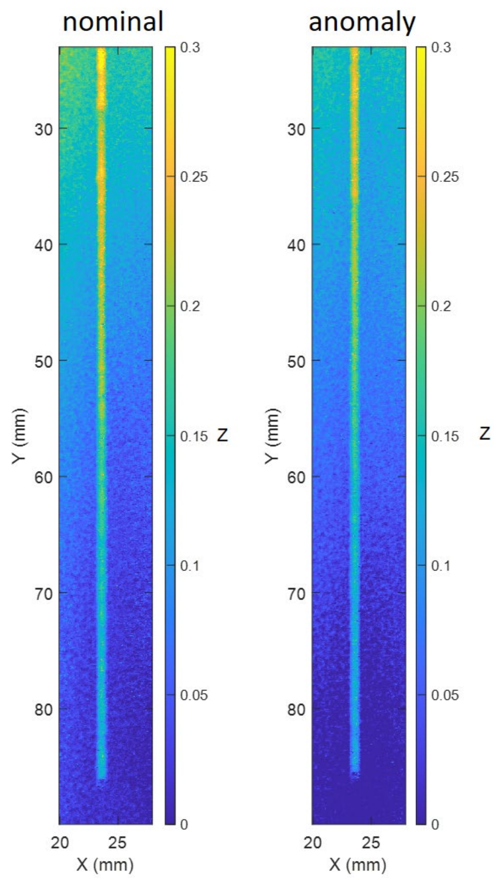

Figure **5-5**: Images of completed single bead depositions (left). Build height data surface plot (right).

The single beads were cross sectioned at three locations along the track length. Each sample was etched and polished. The macro images of the cross sections are shown in Figure 5-6.

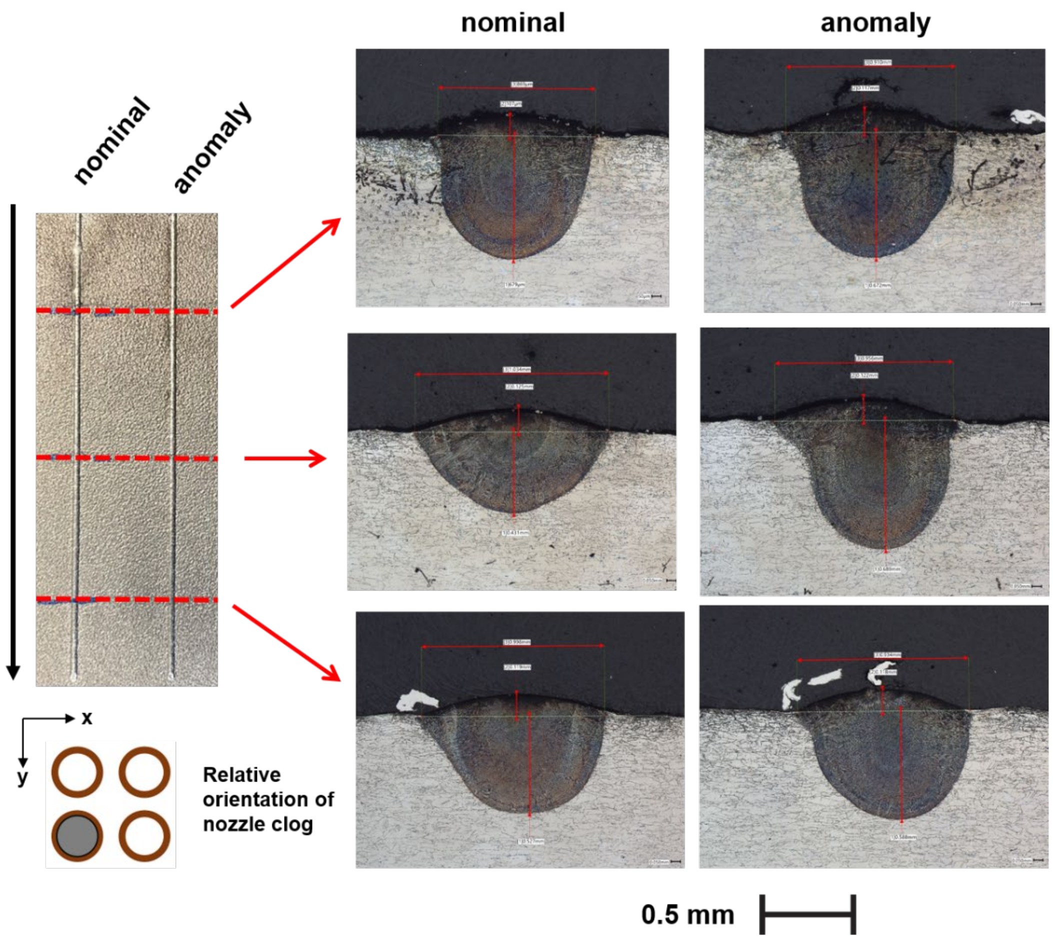

Figure **5-6**: Images of single bead cross sections.

Figure 5-7 shows the outline of the anomaly cross sections overlaid on the nominal cross sections. This illustration makes it very clear that the middle cross section for the nominal bead has a much shorter penetration depth than the anomaly bead.

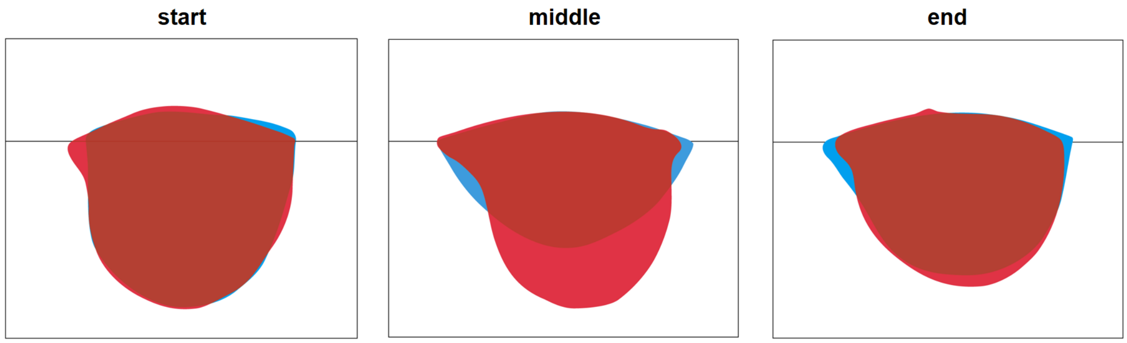

Figure **5-7**: Illustration comparing cross sections of single beads. Nominal: blue, anomaly: red.

To further compare the two single beads, the dilution of each cross section was calculated. Dilution is the ratio of melted substrate to the total melted area,

$$D = \frac{A_m}{A_c + A_m} \tag{1}$$

where A_m is the area of the molten penetration or heat affected zone, and A_c is the area of the clad above the substrate as shown in Figure 5-8. The areas were measured in Adobe Photoshop with the area measurement tool. The dilution values for these cross sections are very high compared to common DED depositions [48]. No clear effect from the forced nozzle clog on the geometry of this single bead was observed as shown in Table 5-1.

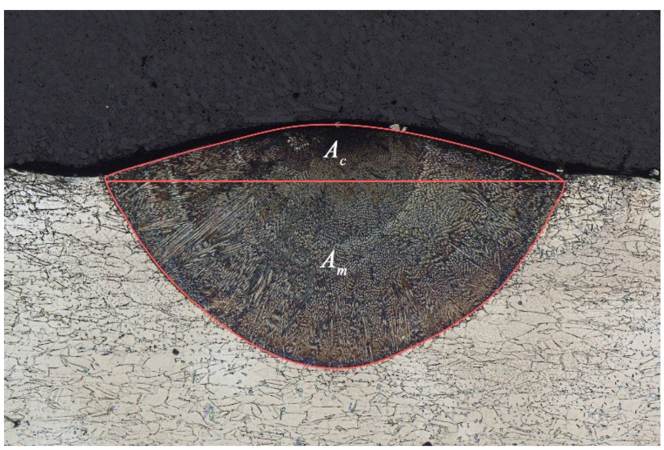

Figure **5-8**: Graphic showing the area of the clad portion, A_c, and the molten portion, A_m, of a single bead cross section.

Table **5-1**: Percent dilution values for each single bead cross section.

	start	**middle**	**end**
nominal	87.82%	78.10%	82.94%
anomaly	85.06%	87.00%	83.81%

5.2.2 Thin Walls

The thin walls were 30 layers tall, however, the deposition direction switched each layer. Therefore, the AFS sensor was only following the laser and scanning the new deposited track for odd layers. The scan and subsequent analysis were performed every two layers. The build height data from nominal and anomaly build were post-processed and filtered using the methods discussed previously. This data after layer 29 is displayed as surface plots in Figure 5-9. There is a clear height difference between the two builds. A cross section of both builds was selected from a slice of data near the middle of the deposition length. The slice of build height data from both builds after layer 19 is shown in Figure 5-9. At layer 19, the anomaly build has processed with the forced clog for four layers.

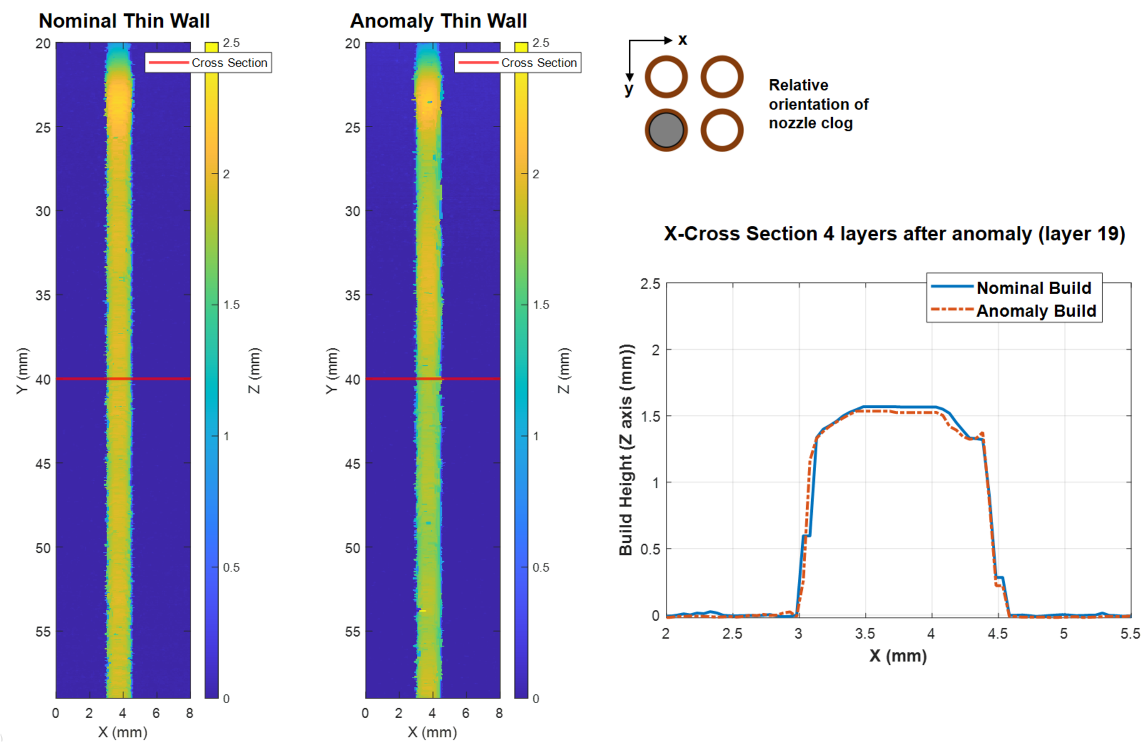

Figure **5-9**: Deposition height surface plot after layer 29 for both thin wall builds (left). Cross section from the middle of the track at Layer 19, four layers after the intentional nozzle clog (right).

The flow rate data from the calibrated PFM sensor is shown in Figure 5-10a. The flow rate is shown to be near the set value, but drastically decreases to 75% of the initial rate once the nozzle clog has been implemented, i.e. after layer 10. The percentage of detections in quadrant 3 also exhibited a significant decrease in percentage after the nozzle clog as shown in Figure 5-10b.

To find the maximum height of the cross section, ± 5 points around the maximum point were averaged. The average maximum height was calculated for every two layers at the same cross section location. This was completed for both the nominal and anomaly build. Figure 5-10c displays the change in build height with increase in layer. The nozzle clog was implemented between layers 10 and 11. After the nozzle is intentionally clogged, the rate of the height increase is smaller for the anomaly build than the nominal build. The percent error of the anomaly build height to the nominal height build height at layer 19 (after processing four layers with the anomaly) is 2.5%.

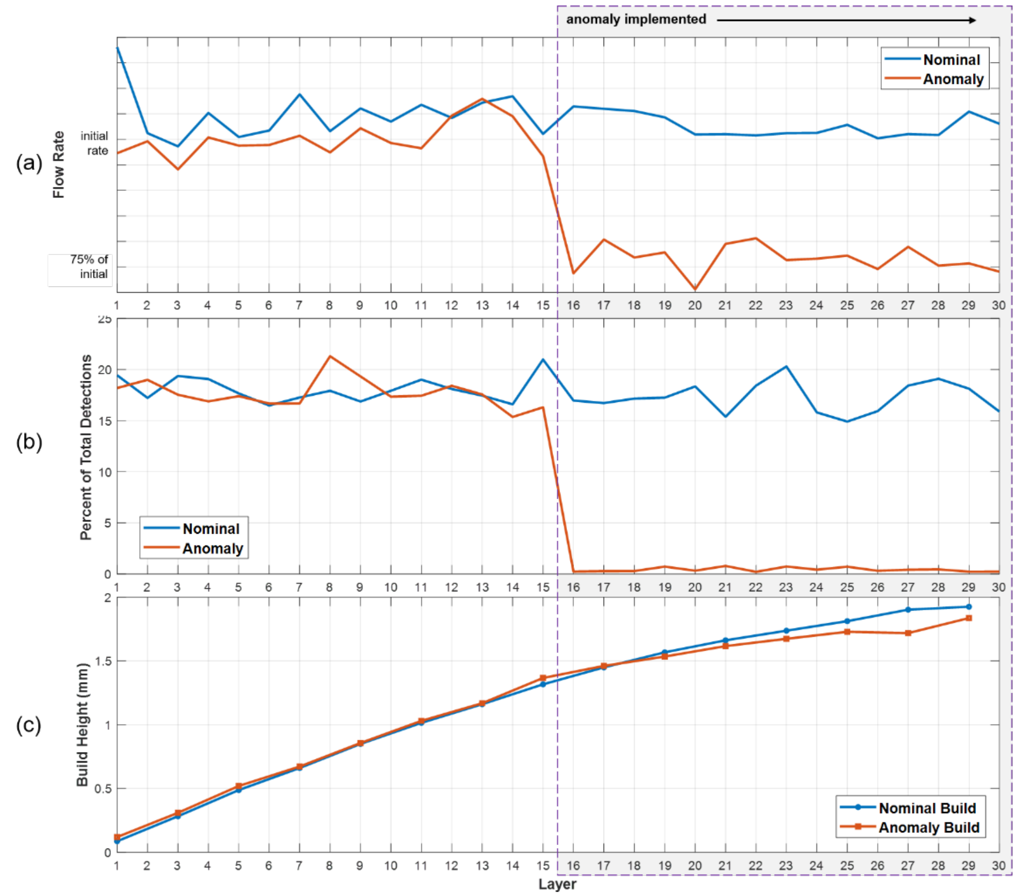

Figure **5-10**: Thin wall full nozzle blockage: (a) Flow rate vs Layer. (b) Percentage of Third Quadrant Detections vs Layer. (c) Build height vs Layer.

5.2.3 Pads

The pad builds were 10 tracks wide, alternating deposition direction with each track. The AFS only captured the newly deposited tracks for the odd tracks moving in the positive y direction. To observe the average height of each layer, the ninth hatch scan was used, when each layer was almost complete. The build height data at the end of both the nominal and anomaly pad builds are displayed in surface plots in Figure 5-11. The color scale shows that the anomaly pad is shorter than the nominal pad. A slice of build height data from layer 14 was selected near the beginning of the build and displayed on a plot with height on the y axis. Layer 14 was four layers after the clog was implemented. The percent error between the anomaly build height and nominal build height at layer 14 is about 6.91%.

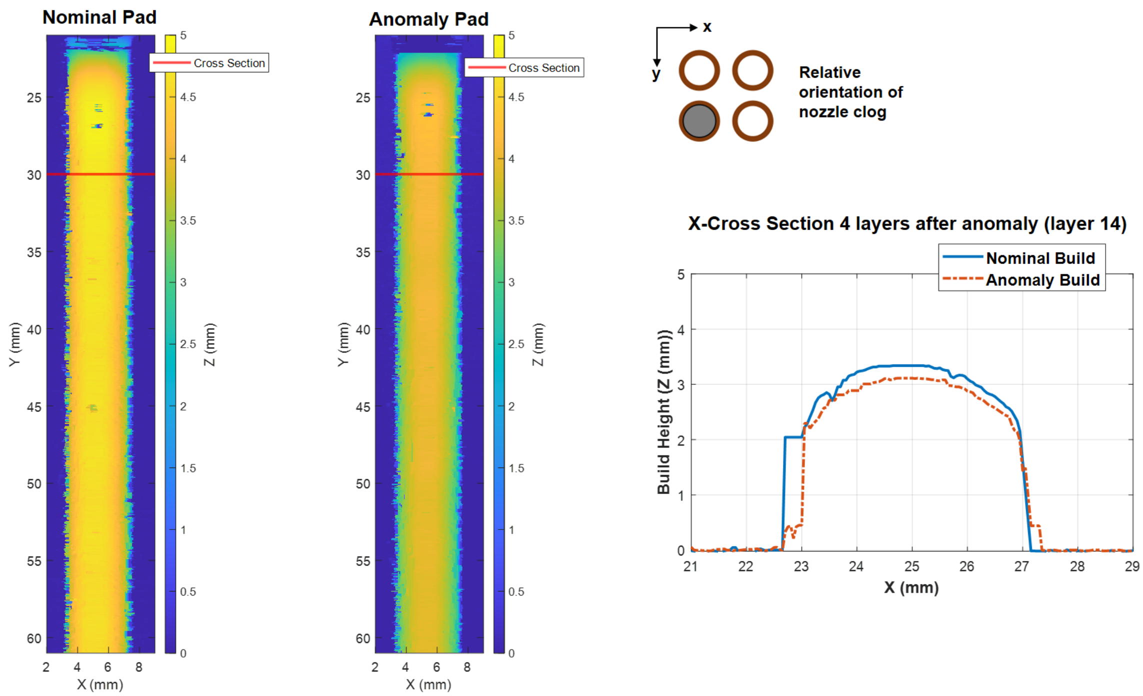

Figure **5-11**: Deposition height surface plot after layer 20 of both pad builds (left). Cross section of the builds at layer 14 (right).

The flow rates over the course of the builds are shown in Figure 5-12a. The PC running the LabVIEW program experienced during the experiment causing the files for layers 14 and 15 to be corrupt. For the plots in Figure 5-12a and b, layers 14 and 15 were filled in using a nearest neighbor method in MATLAB. The flow rate of the anomaly pad starts above the set flow rate with the nominal flow, reduces after the clog was introduced. Additionally, the percent of third quadrant detections is shown to have a significant effect from the clog in Figure 5-12b.

The average height of the cross section was calculated once for each layer and displayed on a plot in Figure 5-12c. The increase in height for the nominal pad follows a linear trend. Once the nozzle clog has been implemented after layer 10, the anomaly build increase in build height is reduced significantly.

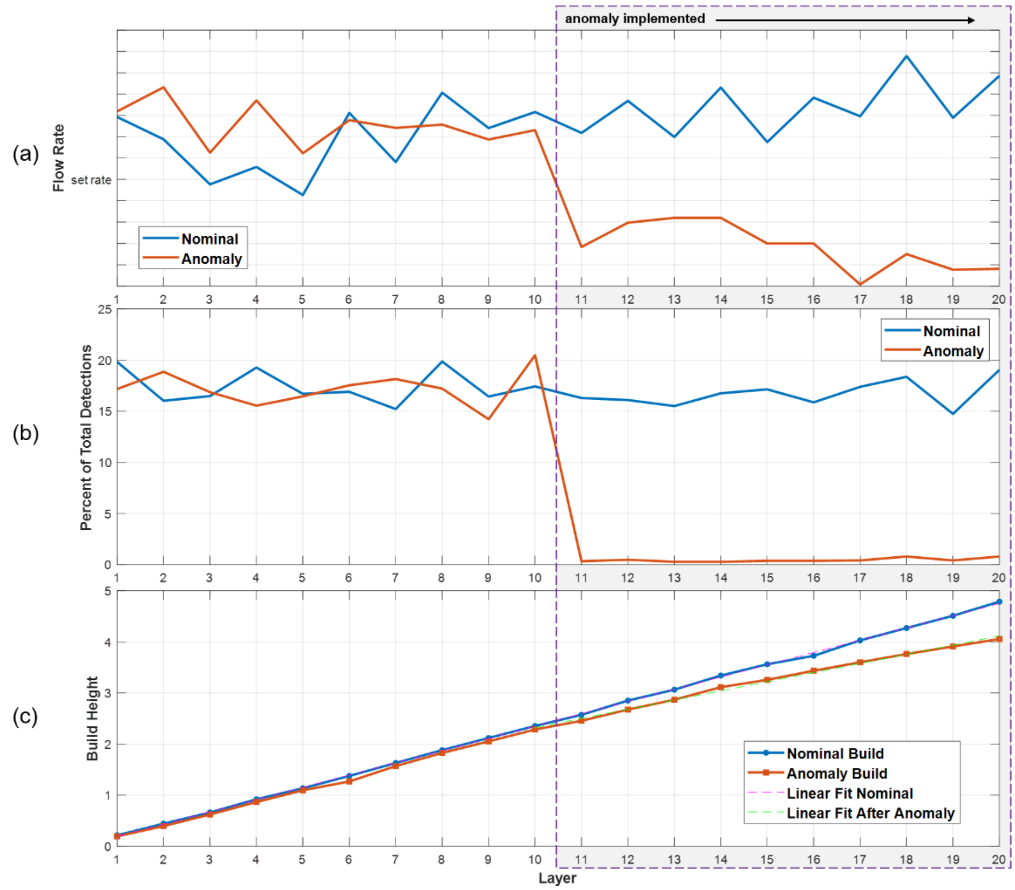

Figure **5-12**: Pad full nozzle blockage: (a) Flow rate vs Layer. (b) Percentage of Third Quadrant Detections vs Layer. (c) Build height vs Layer.

5.2.4 Airfoils

The build height data for the nominal and anomaly airfoil builds are shown at the last layer in Figure 5-13. The color of the builds indicates that the height of the nominal airfoil is greater than the height of the anomaly airfoil. A slice of height data was selected near the start of the airfoil as an x cross section. The slice of data from layer 14 is displayed in Figure 5-13. At layer 14, the anomaly had been present for four layers. The percent error of the anomaly build height at layer 14 is 7.7%.

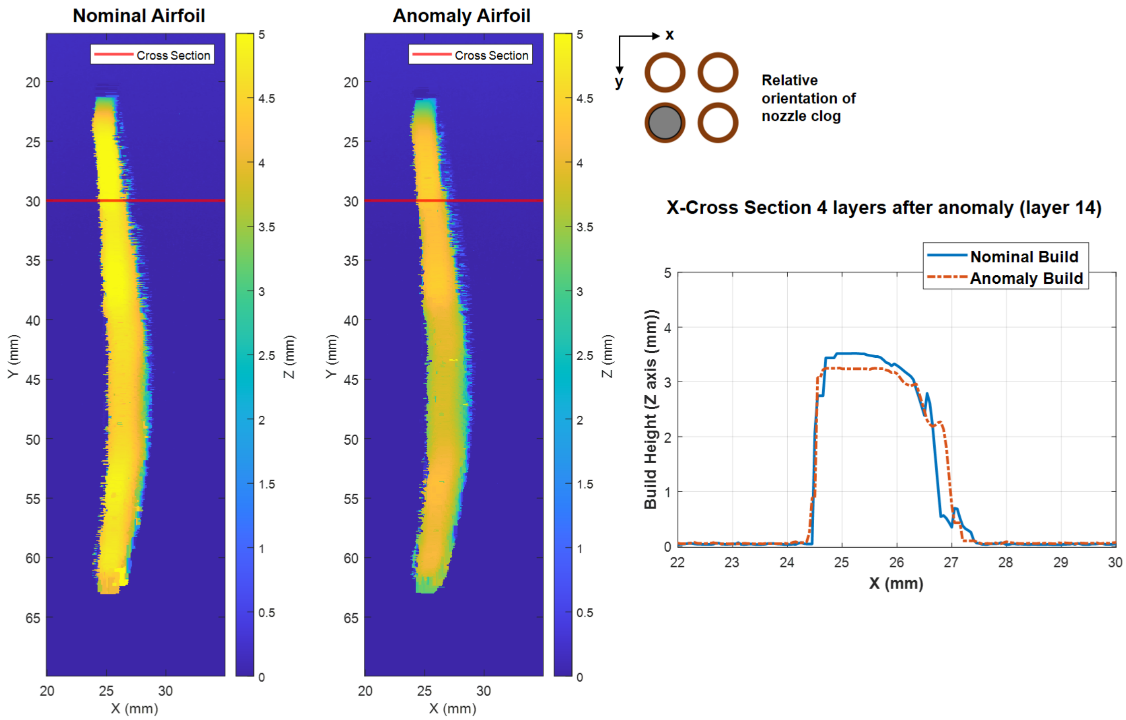

Figure **5-13**: Deposition height surface plot after layer 20 of both builds (left). Cross section at y = 30 mm from layer 14.

The PC running the PFM LabVIEW program experienced an issue during the experiment causing the file for layer 4 to be corrupt. For the plots in Figure 5-14a and 5-14b, layer 4 was filled in using a linear method in MATLAB. The estimated powder flow rate for the nominal flow appears irregular and is possibly an error in the PFM estimation as shown in Figure 5-14a. Further work is needed to understand this behavior. However, the estimated flow rate for the anomaly flow shows a decrease after the clog was implemented. Although the estimated flow rate does not appear correct, the percent of detections in quadrant 3 looks very consistent for the nominal flow as shown in Figure 5-14b.

The average build height at that cross section was calculated for each layer and displayed on the first plot in Figure 5-14c. The nominal airfoil follows a linear trend in deposition height per layer. However, the anomaly airfoil shows a significant decrease in slope after the nozzle clog was implemented.

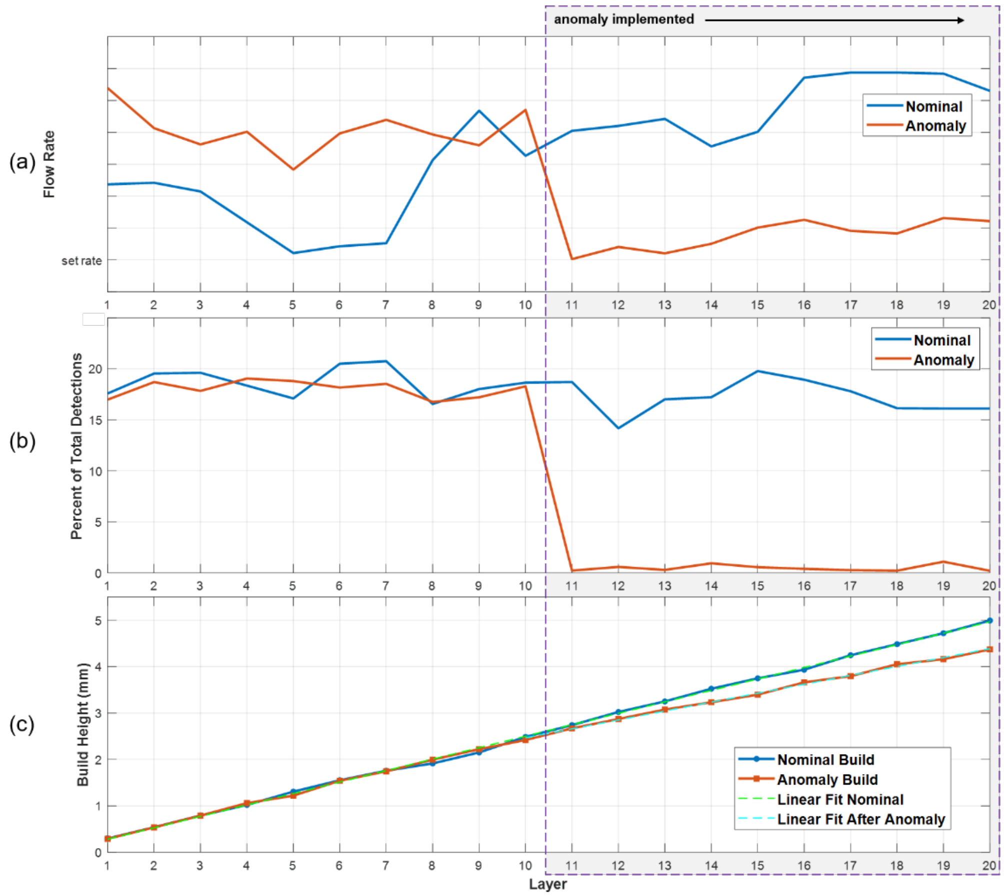

Figure **5-14**: Airfoil full nozzle blockage: (a) Flow rate vs Layer. (b) Percentage of Third Quadrant Detections vs Layer. (c) Build height vs Layer.

5.3 Partial Nozzle Blockage Anomaly Experiment Results

Images of the completed partial nozzle blockage builds are shown in Figure 5-15.

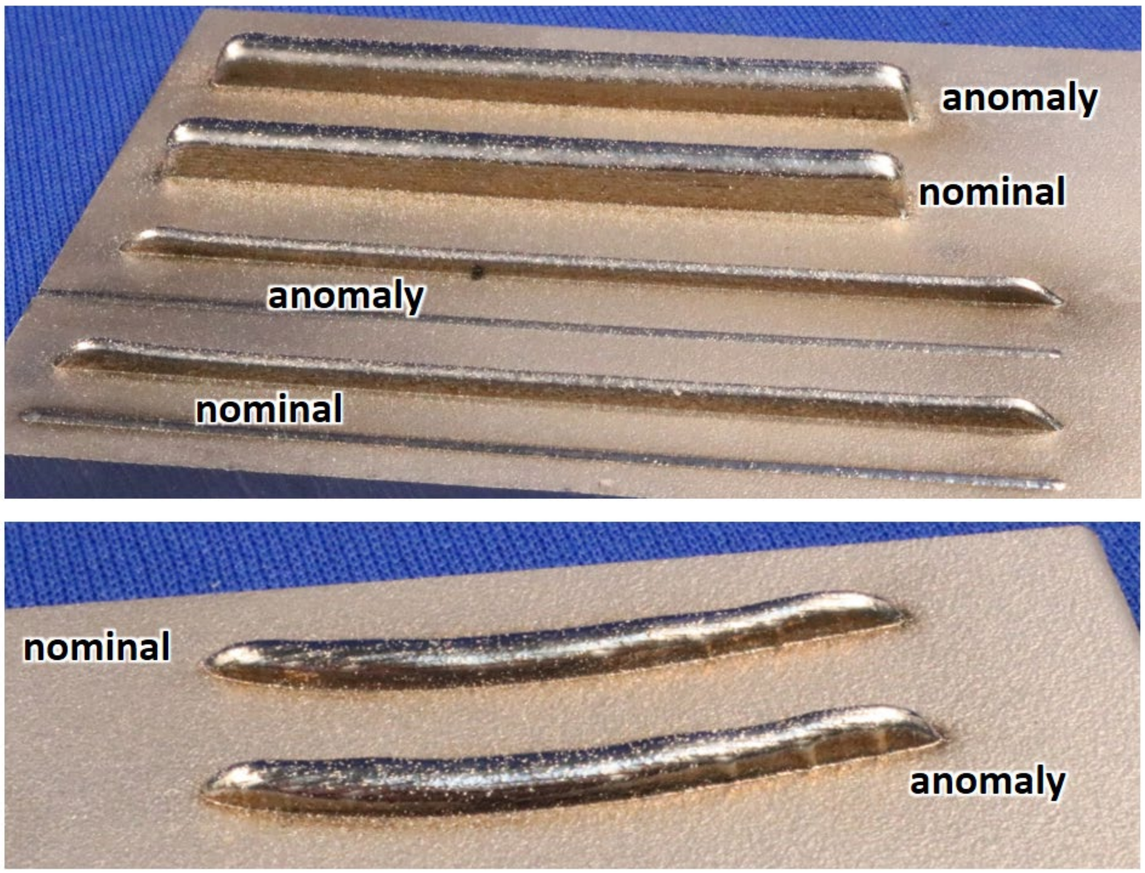

Figure **5-15**: Images of completed partial nozzle blockage builds. From top to bottom: pads, thin walls, airfoils.

The cross section powder flow data from the PFM sensor for the nominal and intentional anomaly conditions are shown in Figure 5-14. It appears the apparatus used to create the partial blockage likely dispersed the powder many directions outward from the nozzle three. The PFM sensor registers these stray particles as being part of the powder flow, yielding an incorrect over-estimate of the powder flow rate.

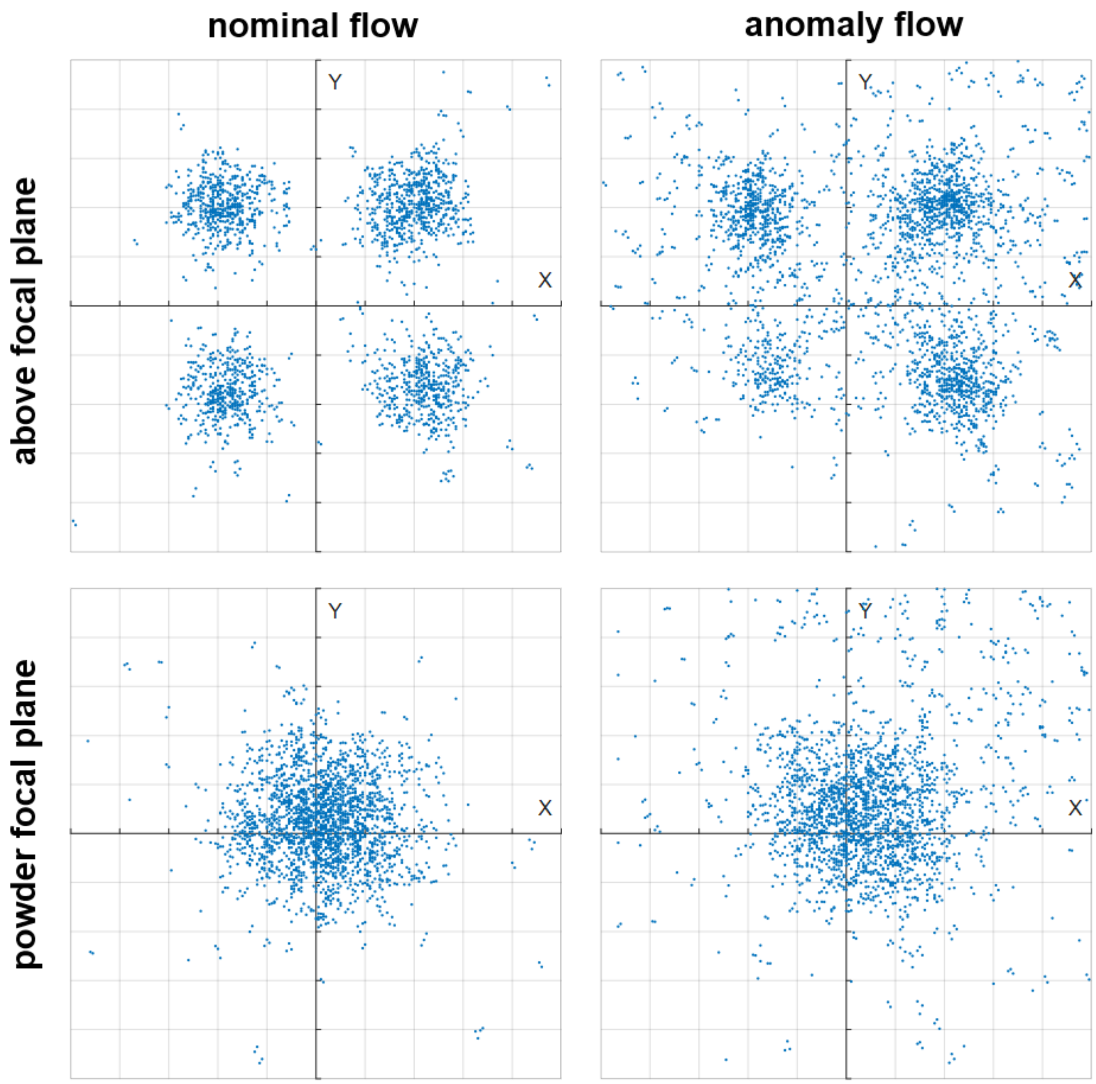

Figure **5-16**: Powder cross section distribution with nominal flow and with nozzle three blocked at and above the focal plane. Each block represents 1 mm.

Because the estimated flow rate was inconsistent, this data was analyzed with an additional method to assess the effect of the anomaly on the powder flow. The data was run through the *k*-means clustering algorithm in MATLAB. The MATLAB *k*-means algorithm uses *k*-means ++ to choose the initial values [47]. With the data and the number of clusters provided by the user as input parameters, the *k*-means method iterates to determine the individual clusters and the centroid of each cluster [42]. The centroid of nozzle three is used to compare the nominal flow to the anomaly flow for each set of partial blockage builds. An example of the *k*-means clustering results are shown in Figure 5-17.

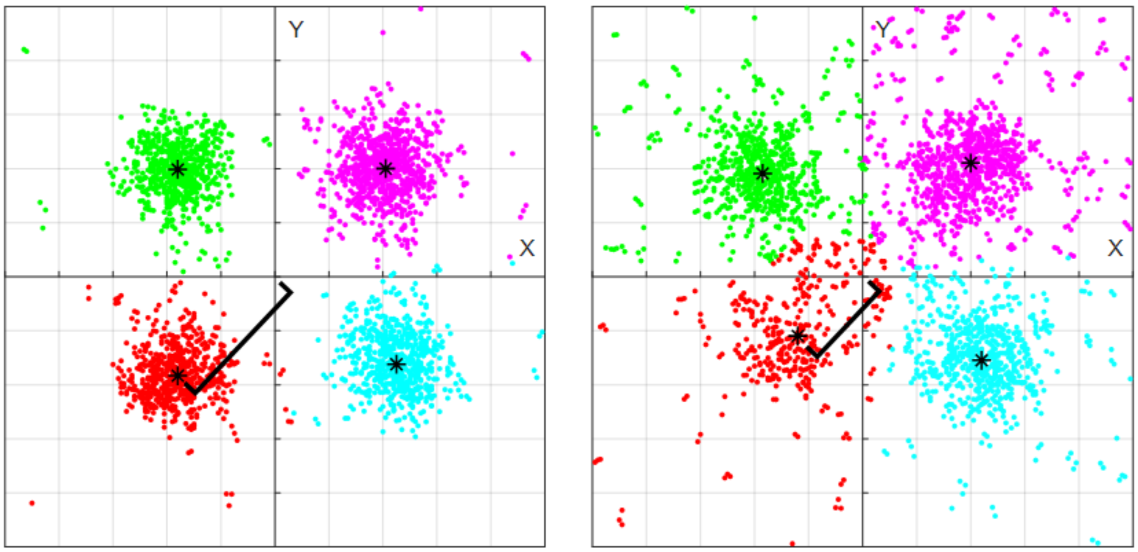

Figure **5-17**: Powder distribution plot of nominal (left) and partial (right) anomaly flow with showing how the centroids determined by the *k*-means method can be used to compare the two flows.

5.3.1 Thin Walls

Because the AFS sensor only records surface topography data following the laser, the build height was only analyzed every other layer. The build height data was filtered in a similar way to the previous builds and then displayed on a surface plot to compare heights visually between builds as shown in Figure 5-18. The anomaly thin wall is shorter than the nominal thin wall. However, both have peaks at the start of the build. A slice of the height data was taken around the middle of the track and observed at layer 19. At this point the anomaly build has processed four layers with the partial blockage implemented. The total build height at layer 19 has a percent error of 7%.

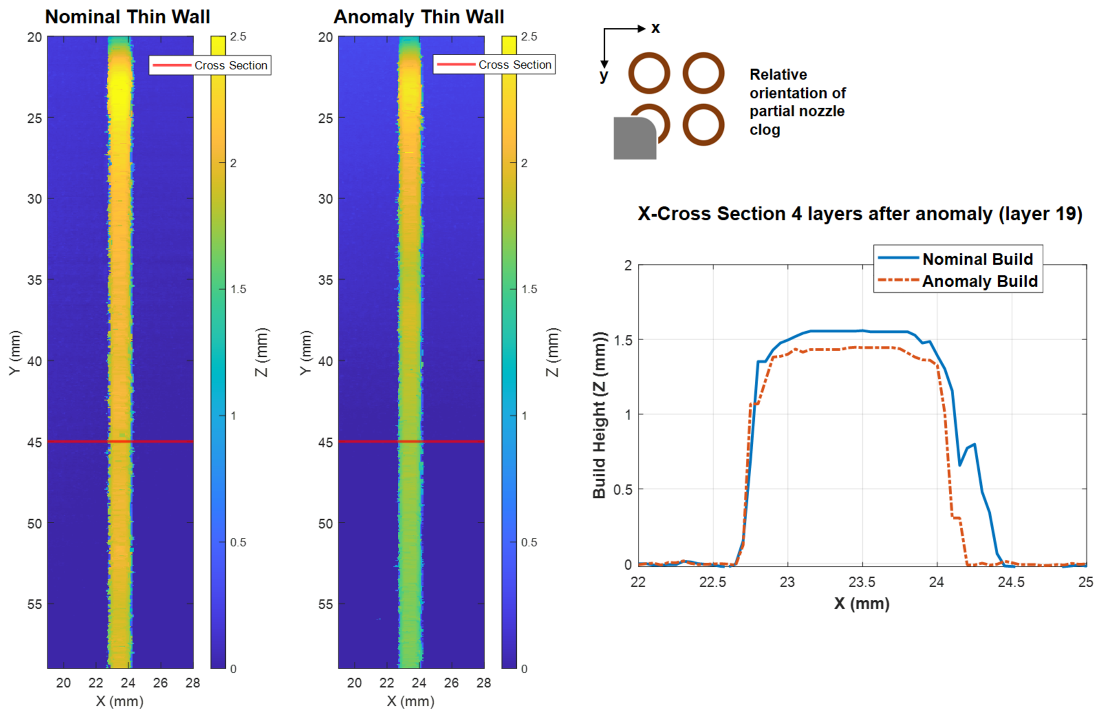

Figure **5-18**: Deposition height surface plot after layer 29 of both thin walls (left). Cross section both builds from y = 45 mm of layer 19.

The estimated flow rate shows that both builds start above the initial flow rate setting, as shown in Figure 5-19a. When the anomaly is introduced, the estimated flow rate appears to increase, as a result of the scattered particles interfering with the PFM sensor. This overestimated flow rate makes it difficult to identify that an anomaly exists from this estimated flow rate data alone. However, the percent of total detections for the third quadrant and the centroid distance of the third nozzle flow show a clear indication of an anomaly when plotted against layer number as shown in Figure 5-19b. The partial anomaly brings the percentage of the third nozzle flow detections from about 20% to about 10%. The centroid location of the third nozzle flow shifts much closer to the center when the anomaly was implemented as shown in Figure 5-19c.

The average maximum height of each build at that cross section as a function of layer are displayed in Figure 5-19d to illustrate the increase in build height with each layer. Neither thin wall follows a linear height increase. This trend indicates that the thin walls are underbuilding as the rate of decreasing layer thickness continues to get worse. Once the partial anomaly has been introduced, the anomaly thin wall height increases at a smaller rate than the nominal build. At the end of the build, there is a significant height difference.

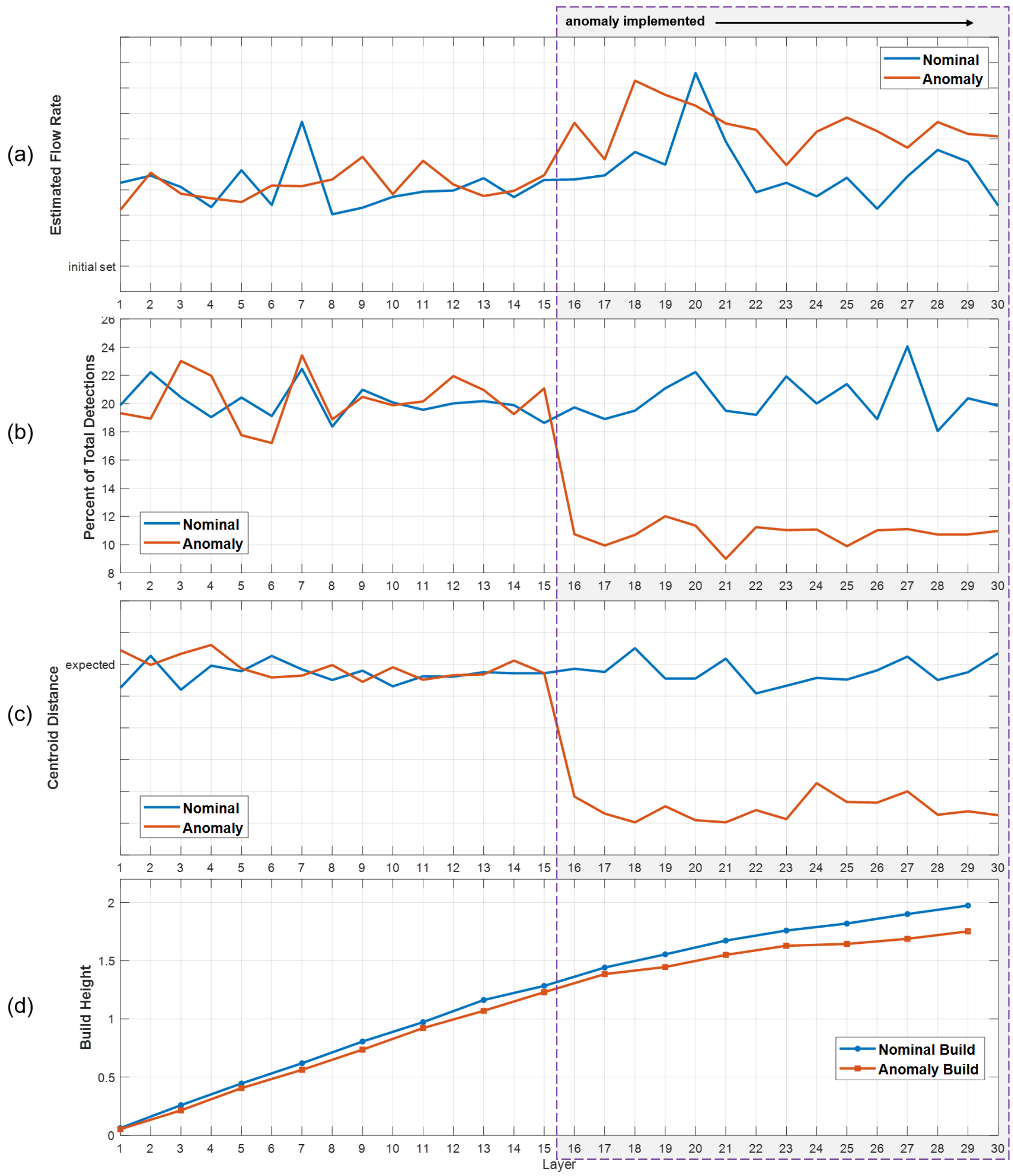

Figure **5-19**: Thin wall partial blockage: (a) Flow rate vs Layer. (b) Percentage of Third Quadrant Detections vs Layer. (c) Centroid distance of Third Quadrant Flow. (d) Build height vs Layer.

5.3.2 Pads

The build height data for the pad builds was filtered using the same method as described for the previous builds. The build height data for the nominal pad is visually taller than the anomaly pad as shown in Figure 5-20. At layer 14, a slice of the build data was analyzed as a cross section. At this point the partial blockage had affected four layers of the anomaly pad. Comparing the maximum height of the two builds at layer 14, the anomaly pad height has a percent error of 6.75%.

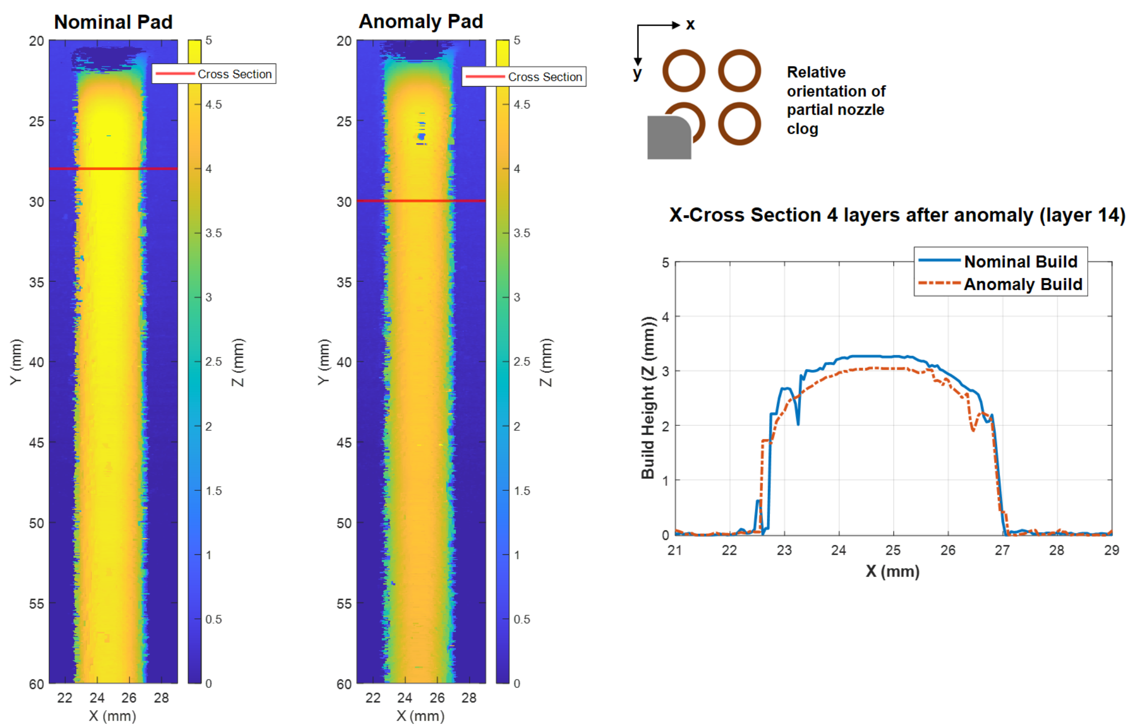

Figure **5-20**: Deposition height surface plot after layer 20 of both builds (left). Cross section at y = 28 mm from layer 14.

The estimated flow rate shows an overestimation after the anomaly was implemented as shown in Figure 5-21a, as well as an irregular powder flow far above the set rate throughout both pad builds. But, the percent of detections and centroid distance for nozzle three provide a clear method to identify the presence of a flow anomaly as shown in Figure 5-21b and Figure 5-21c.

The partial anomaly decreased the percentage of powder particles in quadrant 3 from about 20% to less than 10%. The centroid of the third nozzle flow shifted much closer to the center after the partial anomaly was implemented.

The average maximum build height was calculated for each layer at the same cross section and displayed on plot vs layer in Figure 5-21d. The nominal pad build height plotted as a function of layer followed a linear trend. After the anomaly was introduced following layer 10, the anomaly pad showed a decreased slope but remained linear. By layer 20, there is a significant difference in total build height.

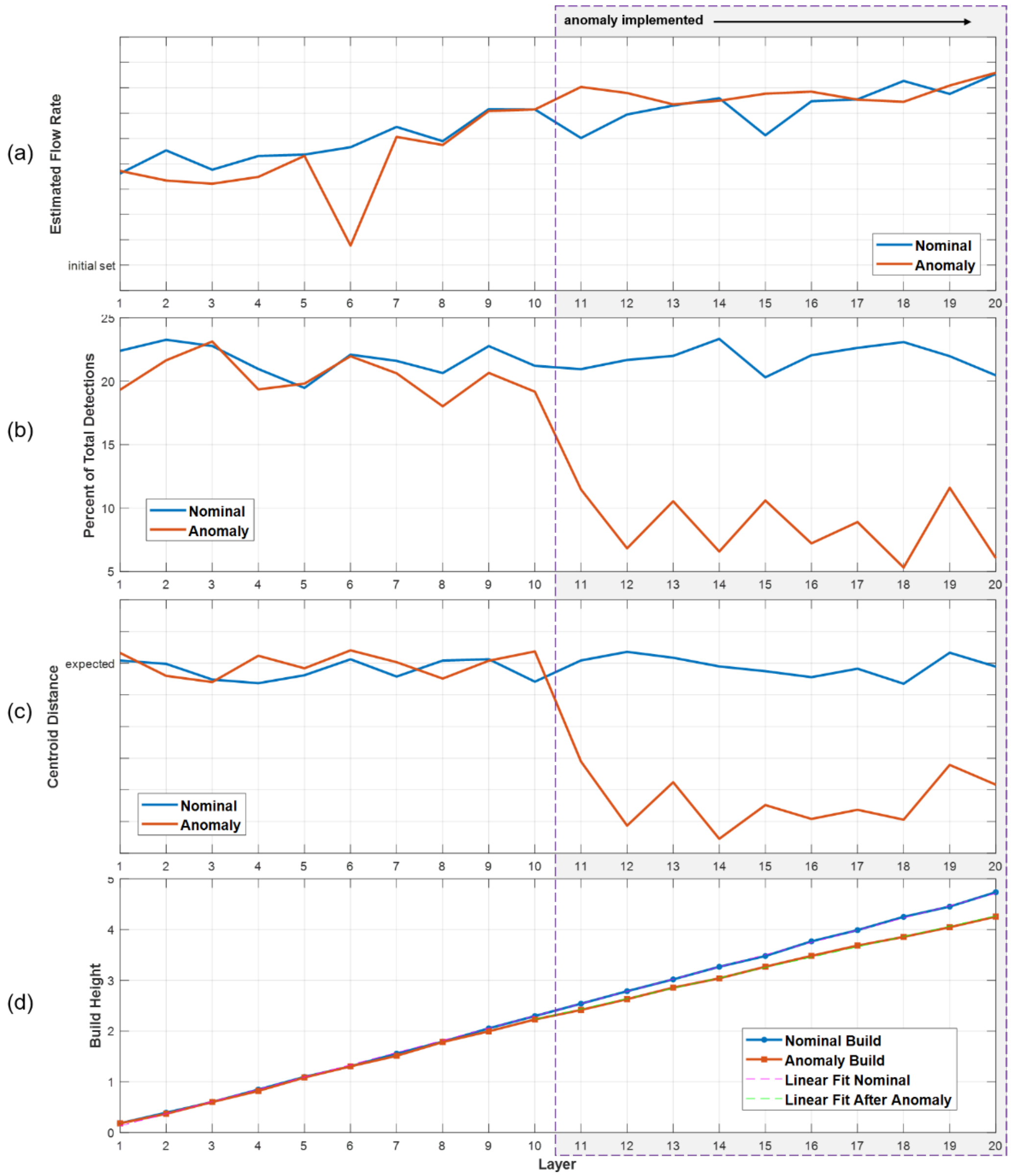

Figure **5-21**: Pad partial blockage: (a) Flow rate vs Layer. (b) Percentage of Third Quadrant Detections vs Layer. (c) Centroid distance of Third Quadrant Flow. (d) Build height vs Layer.

5.3.3 Airfoils

The final topology of both airfoil builds are shown through a surface plot in Figure 5-22. The anomaly airfoil is shorter than the nominal airfoil. A slice of data was taken near y = 30 mm and analyzed as a cross section. The cross section shown in Figure 5-22 is from layer 14, after the anomaly build has processed with the partial blocked nozzle for four layers. The height of the anomaly airfoil at layer 14 has a percent error of 6.77%.

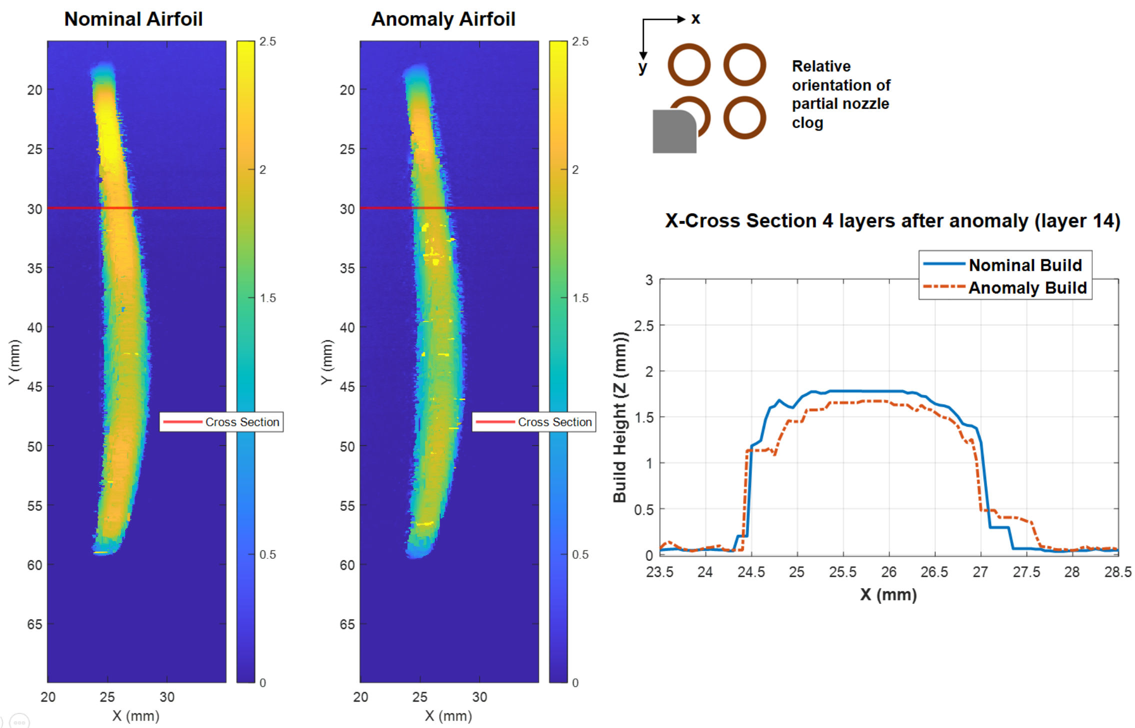

Figure **5-22**: Deposition height surface plot after layer 20 of both builds (left). Cross section at y = 30 mm from layer 14 (right).

The estimated powder flow for these set of builds is mostly inconclusive. The flow rate showed no significant change after the partial anomaly was put in place as shown in Figure 5-23a. On the other hand, the percent of powder detections and the centroid distance both provide clear indications that an anomaly exists in the powder flow as shown in Figure 5-23b and c. The partial anomaly decreased the nozzle 3 flow from about 22% to about 13%. And the partial anomaly shifted the centroid of the nozzle 3 flow closer to the center.

The average maximum build height for the X cross section was calculated for each layer and presented in Figure 5-23d. This plot shows that the nominal airfoil build height was not linear, indicating that it was underbuilding. The underbuilding was likely a result of an external parameter such as irregular laser power. However, the partial anomaly still had a significant affect, causing the airfoil to under build at a faster rate.

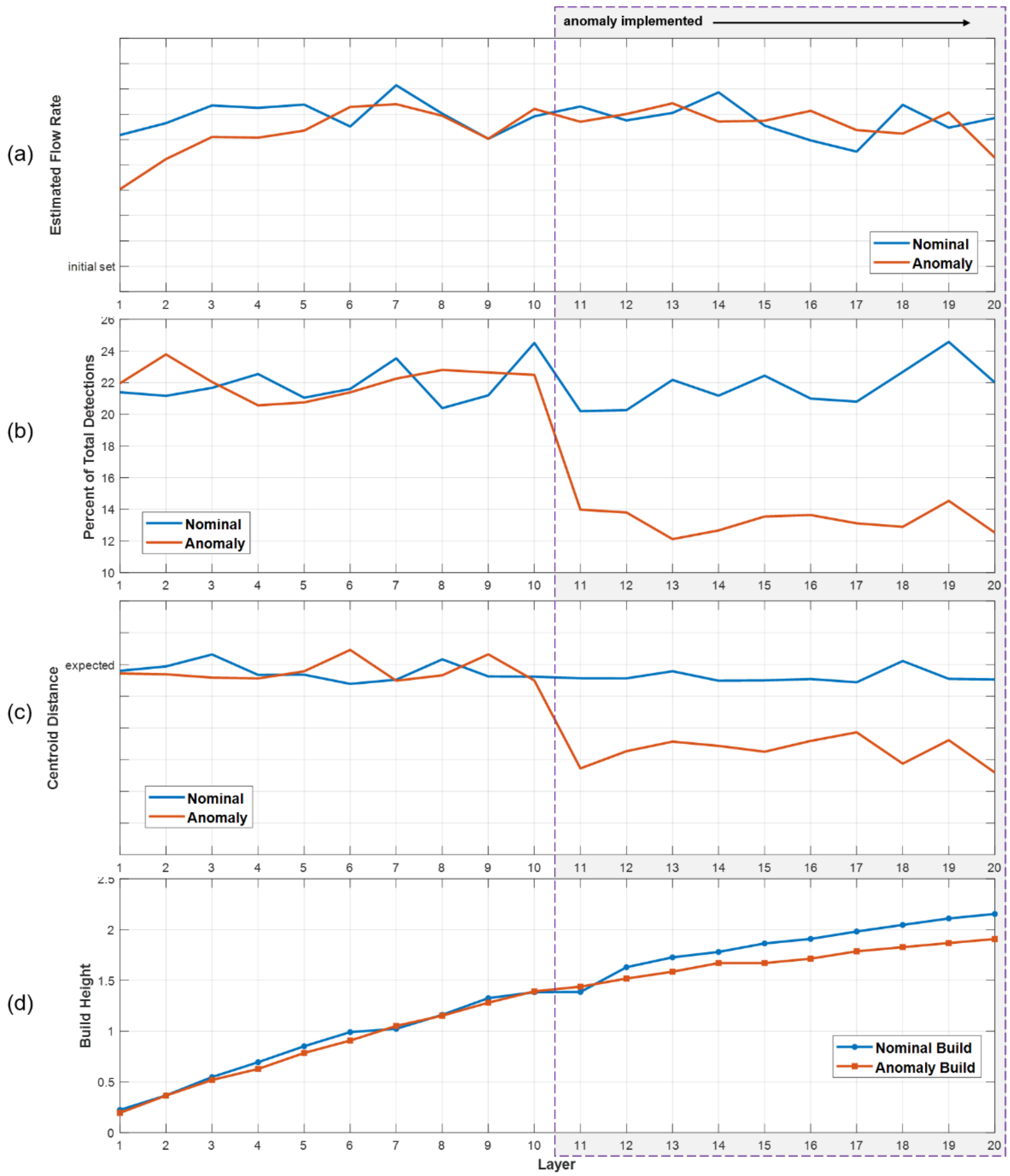

Figure **5-23**: Airfoil partial blockage: (a) Flow rate vs Layer. (b) Percentage of Third Quadrant Detections vs Layer. (c) Centroid distance of Third Quadrant Flow. (d) Build height vs Layer.

5.4 Discussion of Results

The analysis of the build height data from the full and partial nozzle blockage experiments show a direct relationship between powder flow issues and final build quality. The thin walls in both experiments experienced underbuilding and the forced blockage increased the rate of underbuilding. The nominal pads for both experiments built as expected, and the anomaly pads yielded a significantly decreased rate of build height. The airfoil builds represented a realistic build application and the nozzle blockages that were introduced had a significant impact on build height in both experiments. Table 5-2 shows that after only four layers of processing with a nozzle blockage, noticeable build height errors are already present. And in the case of a prolonged, unnoticed powder flow anomaly for 10 layers, the percent error of build height is significant.

Table **5-2**: Build height reduction after four and ten layers following an introduced nozzle blockage.

	Anomaly Present	**Thin Wall**	**Pad**	**Airfoil**
Full Blockage	*4 Layers*	2.55%	6.91%	7.69%
	10 Layers	6.32%	13.84%	12.22%
Partial Blockage	*4 Layers*	7.10%	6.75%	6.78%
	10 Layers	9.89%	10.34%	11.16%

The analysis of powder flow in these forced nozzle blockage experiments, demonstrated that the PFM can be used to measure and monitor powder flow using a variety of different methods. The x-y distribution of the powder flow can be used to visualize the effect of a powder flow anomaly from a specific nozzle. This distribution was analyzed and reduced to a single metric in many ways, but the simplicity of the percentage of detections in each quadrant clearly shows when a single nozzle anomaly exists. The use of the k-means algorithm to determine centroids provided additional information to characterize powder flow from each nozzle, and was shown to be strongly influenced by partial nozzle blockages.

There are several possible sources of error that occurred over the course of both experiments. The PFM sensor did not accurately register the expected change in powder flow rate for the partial blockage experiment. This inaccuracy was likely a result of the flat metal piece used to block part of the flow from nozzle 3 actually directing the powder flow from the nozzle toward the other powder flows. Since the deflected powder would be moving in a more horizontal direction out of the powder stream area, it may have been caught as a "detection" by the PFM sensor, resulting in an incorrect higher estimate of powder flow rate. The PFM Calibration might miss some powder in the collection container leading to an incorrect scale measurement. This calibration method inaccuracy might contribute to the wide 95% prediction interval shown in Figure 5-1. In addition the coaxial gas may interfere with an accurate scale reading because it is aimed directly at the scale tray.

Chapter 6

Summary and Future Work

This study presented the development and validation of a powder flow monitoring system used to detect powder flow anomalies through a set of forced anomaly experiments in which a nozzle was fully or partially blocked in a systematic way. Powder flow for the emulated blockages was characterized, and found to provide a realistic representation of naturally occurring blockages. These experiments show that developed powder flow metrics can detect a partial or full nozzle blockage, and further provide evidence of the direct relationship of specific powder flow anomalies to in-situ and final build quality.

The powder flow monitoring system includes a developed calibration method for estimating flow rate, and an in-situ analysis program that is able to detect powder flow anomalies using a variety of metrics. The calibration method yields a conversion value that can be used to estimate the powder flow rate between layers. The in-situ analysis used the horizontal distribution of the powder flow data to identify when flow from a particular nozzle fell outside user defined limits. This system provides an ability to monitor DED processes more closely using quantifiable metrics, and will aid in preventing powder flow anomalies that could impact build quality from going unnoticed by a human operator.

A complete single nozzle clog (on a four-nozzle system) was shown to directly reduce powder flow rate to nearly 75% of the nominal rate for low flow rates. The forced nozzle clog was also shown to cause a significant reduction in layer thickness. A partial blockage of one nozzle, representing agglomerated spatter adhering to the nozzle, was shown to cause a reduction in density of powder flow on the side of the blockage. The powder flow distribution at the working distance was shown to be uneven as a result of the partial blockage. That partial blockage was also shown to affect the build height in-situ and at the end of the build.

There are several opportunities for future development that could improve the accuracy of PFM or provide more insight to the relationships between DED powder flow and build quality. The thin wall, pad and airfoil builds should each be cross sectioned to observe the effect of powder flow anomalies on the grain structure of the reduced layers. Studying the grain structure could inform whether underbuilding as a result of a powder flow blockage yields poor build quality. The PFM calibration method could be improved to be more accurate at low flow rates by using better weight measurement equipment or by improving the experimental set up to ensure all the powder is accounted for. Additionally, increasing the number of runs for calibration, over a wider range of flow rates, may improve the prediction interval. Future work could realize closed loop control based on PFM analysis, either to automatically pause a build or to move the nozzles with material adhesion to a cleaning station. This effort only observed the effects of an anomaly on one nozzle. Future work could extend this to include varying the position of the anomaly or implementing more than one anomaly, and relating the effect of deposition direction as it relates to anomaly position. It is recommended to investigate the robustness of recovery from a powder flow anomaly, to determine under what conditions recovery of build quality is possible. Furthermore, future work should include observing the powder flow rate of individual nozzles during a prolonged clog, as the internal clog increases, it could be possible for the flow rate to recover through the unblocked nozzles. Several methods for detecting a powder flow anomaly were developed during this work. Powder capture efficiency could be an additional metric to observe and further relate irregular powder flow to build quality. Given that the experiments conducted in this study used very low flow rates compared to common DED practice, future work could investigate the impact of powder flow anomalies at higher flow rates seen in other industries. In this work, PFM was used to study powder flow rate and observe powder flow anomalies. However, the PFM system is capable of much more and could be used as a tool to observe other parameters affecting powder flow behavior.

This work has developed and validated a powder characterization calibration strategy, introduced two new powder flow metrics, and has related these metrics to final build quality. The PFM data were able to be directly observed alongside the build height data, showing exactly when the anomaly "occurred" and quantifying how the build height was affected. The use of in-situ powder flow monitoring is a critical technology to aid in improving the reliability of the DED process.

References

[1] C. Atwood *et al.*, "Laser engineered net shaping (LENS^{TM}): A tool for direct fabrication of metal parts," in *International Congress on Applications of Lasers & Electro-Optics*, Orlando, Florida, USA, 1998, pp. E1–E7. doi: 10.2351/1.5059147.

[2] "ASTM F3187 Standard Guide for Directed Energy Deposition of Metals." ASTM International, West Conshohocken, PA, Nov. 2016. [Online]. Available: www.astm.org

[3] R. Huang *et al.*, "Energy and emissions saving potential of additive manufacturing: the case of lightweight aircraft components," *J. Clean. Prod.*, vol. 135, pp. 1559–1570, Nov. 2016, doi: 10.1016/j.jclepro.2015.04.109.

[4] R. Huang *et al.*, "Environmental and Economic Implications of Distributed Additive Manufacturing: The Case of Injection Mold Tooling," *J. Ind. Ecol.*, vol. 21, no. S1, Nov. 2017, doi: 10.1111/jiec.12641.

[5] J. Bennett *et al.*, "Repairing Automotive Dies With Directed Energy Deposition: Industrial Application and Life Cycle Analysis," *J. Manuf. Sci. Eng.*, vol. 141, no. 2, p. 021019, Feb. 2019, doi: 10.1115/1.4042078.

[6] D. Svetlizky *et al.*, "Directed energy deposition (DED) additive manufacturing: Physical characteristics, defects, challenges and applications," *Mater. Today*, vol. 49, pp. 271–295, Oct. 2021, doi: 10.1016/j.mattod.2021.03.020.

[7] F. S. H. B. Freeman, B. Thomas, L. Chechik, and I. Todd, "Multi-faceted monitoring of powder flow rate variability in directed energy deposition," *Addit. Manuf. Lett.*, vol. 2, p. 100024, Apr. 2022, doi: 10.1016/j.addlet.2021.100024.

[8] Z. Tang *et al.*, "A review on in situ monitoring technology for directed energy deposition of metals," *Int. J. Adv. Manuf. Technol.*, vol. 108, no. 11–12, pp. 3437–3463, Jun. 2020, doi: 10.1007/s00170-020-05569-3.

[9] G. Bi, A. Gasser, K. Wissenbach, A. Drenker, and R. Poprawe, "Identification and qualification of temperature signal for monitoring and control in laser cladding," *Opt. Lasers Eng.*, vol. 44, no. 12, pp. 1348–1359, Dec. 2006, doi: 10.1016/j.optlaseng.2006.01.009.

[10] D. Hu and R. Kovacevic, "Sensing, modeling and control for laser-based additive manufacturing," *Int. J. Mach. Tools Manuf.*, vol. 43, no. 1, pp. 51–60, Jan. 2003, doi: 10.1016/S0890-6955(02)00163-3.

[11] J. T. Hofman, B. Pathiraj, J. van Dijk, D. F. de Lange, and J. Meijer, "A camera based feedback control strategy for the laser cladding process," *J. Mater. Process. Technol.*, vol. 212, no. 11, pp. 2455–2462, Nov. 2012, doi: 10.1016/j.jmatprotec.2012.06.027.

[12] D. A. Kriczky, J. Irwin, E. W. Reutzel, P. Michaleris, A. R. Nassar, and J. Craig, "3D spatial reconstruction of thermal characteristics in directed energy deposition through optical thermal imaging," *J. Mater. Process. Technol.*, vol. 221, pp. 172–186, Jul. 2015, doi: 10.1016/j.jmatprotec.2015.02.021.

[13] P. Zhang, X. Zhou, W. Zhang, T. Zhang, G. Ding, and X. Cheng, "Effects of melt-pool geometry on the oriented to misoriented transition in directed energy deposition of a single-crystal superalloy," *Addit. Manuf.*, vol. 60, p. 103253, Dec. 2022, doi: 10.1016/j.addma.2022.103253.

[14] C. B. Stutzman, A. R. Nassar, and E. W. Reutzel, "Multi-sensor investigations of optical emissions and their relations to directed energy deposition processes and quality," *Addit. Manuf.*, vol. 21, pp. 333–339, May 2018, doi: 10.1016/j.addma.2018.03.017.

[15] A. R. Nassar, B. Starr, and E. W. Reutzel, "Process monitoring of directed-energy deposition of Inconel-718 via plume imaging," presented at the 26th Annual International Solid

Freeform Fabrication Symposium - An Additive Manufacturing Conference, SFF 2015, 2020.

[16] A. Kisielewicz, E. Sadeghi, F. Sikström, A.-K. Christiansson, G. Palumbo, and A. Ancona, “In-process spectroscopic detection of chromium loss during Directed Energy Deposition of alloy 718,” *Mater. Des.*, vol. 186, p. 108317, Jan. 2020, doi: 10.1016/j.matdes.2019.108317.

[17] P. M. Sammons, M. L. Gegel, D. A. Bristow, and R. G. Landers, “Repetitive Process Control of Additive Manufacturing With Application to Laser Metal Deposition,” *IEEE Trans. Control Syst. Technol.*, vol. 27, no. 2, pp. 566–575, Mar. 2019, doi: 10.1109/TCST.2017.2781653.

[18] L. Chen, X. Yao, P. Xu, S. K. Moon, and G. Bi, “Rapid surface defect identification for additive manufacturing with in-situ point cloud processing and machine learning,” *Virtual Phys. Prototyp.*, vol. 16, no. 1, pp. 50–67, Jan. 2021, doi: 10.1080/17452759.2020.1832695.

[19] L. Tang and R. G. Landers, “Layer-to-Layer Height Control for Laser Metal Deposition Process,” *J. Manuf. Sci. Eng.*, vol. 133, no. 2, p. 021009, Apr. 2011, doi: 10.1115/1.4003691.

[20] J. Choi and Y. Chang, “Characteristics of laser aided direct metal/material deposition process for tool steel,” *Int. J. Mach. Tools Manuf.*, vol. 45, no. 4–5, pp. 597–607, Apr. 2005, doi: 10.1016/j.ijmachtools.2004.08.014.

[21] J. C. Haley, B. Zheng, U. S. Bertoli, A. D. Dupuy, J. M. Schoenung, and E. J. Lavernia, “Working distance passive stability in laser directed energy deposition additive manufacturing,” *Mater. Des.*, vol. 161, pp. 86–94, Jan. 2019, doi: 10.1016/j.matdes.2018.11.021.

[22] S. Donadello, V. Furlan, A. G. Demir, and B. Previtali, “Interplay between powder catchment efficiency and layer height in self-stabilized laser metal deposition,” *Opt. Lasers Eng.*, vol. 149, Feb. 2022, doi: 10.1016/j.optlaseng.2021.106817.

[23] X. X. Yao, J. Y. Li, Y. F. Wang, X. Gao, T. Li, and Z. Zhang, “Experimental and numerical studies of nozzle effect on powder flow behaviors in directed energy deposition additive manufacturing,” *Int. J. Mech. Sci.*, vol. 210, p. 106740, Nov. 2021, doi: 10.1016/j.ijmecsci.2021.106740.

[24] S. Takemura, R. Koike, Y. Kakinuma, Y. Sato, and Y. Oda, “Design of powder nozzle for high resource efficiency in directed energy deposition based on computational fluid dynamics simulation,” *Int. J. Adv. Manuf. Technol.*, vol. 105, no. 10, pp. 4107–4121, Dec. 2019, doi: 10.1007/s00170-019-03552-1.

[25] H. Lee *et al.*, “Deep learning for in-situ powder stream fault detection in directed energy deposition process,” *J. Manuf. Syst.*, vol. 62, pp. 575–587, Jan. 2022, doi: 10.1016/j.jmsy.2022.01.013.

[26] C. Kledwig, H. Perfahl, M. Reisacher, F. Brückner, J. Bliedtner, and C. Leyens, “Image-based algorithm for nozzle adhesion detection in powder-fed directed-energy deposition,” *J. Laser Appl.*, vol. 32, no. 2, p. 022021, May 2020, doi: 10.2351/7.0000070.

[27] J. K. Kelly, “Direct-Metal-Deposition (DMD) Nozzle Fault Detection Using Temperature Measurements,” U.S. Patent No. 6,423,926 B1, Jul. 23, 2002

[28] S. W. Brown, A. G. Przyjemski, M. B. McPherson, J. H. Steinberg, D. Corbin, and E. T. W. Reutzel, “Insights into powder flow characterization methods for directed energy distribution additive manufacturing systems,” presented at the Solid Freeform Fabrication 2018: Proceedings of the 29th Annual International Solid Freeform Fabrication Symposium - An Additive Manufacturing Conference, SFF 2018, 2018, pp. 1976–1988. [Online]. Available: https://www.scopus.com/inward/record.uri?eid=2-s2.0-85084960754&partnerID=40&md5=f6966e44f8010c01ec8e4b570fbba2e1

[29] V. Petrovic-Filipovic, R. Görgl, M. Suppan, J. Hesse, and W. Waldhauser, “Monitoring concept for powder flow monitoring in Laser-Directed Energy Deposition (L-DED) process

based on flexible piezoelectric sensors," *Mater. Open Res.*, vol. 1, p. 1, May 2022, doi: 10.12688/materialsopenres.17427.1.
[30] J. Whiting, A. Springer, and F. Sciammarella, "Real-time acoustic emission monitoring of powder mass flow rate for directed energy deposition," *Addit. Manuf.*, vol. 23, pp. 312–318, Oct. 2018, doi: 10.1016/j.addma.2018.08.015.
[31] K. Odum, M. Soshi, and K. Yamazaki, "Numerical Study of Material Selection for Optimal Directed Energy Deposition Single Nozzle Powder Efficiency," *J. Manuf. Sci. Eng.*, vol. 144, no. 12, p. 121006, Dec. 2022, doi: 10.1115/1.4054937.
[32] S. Y. Wen, Y. C. Shin, J. Y. Murthy, and P. E. Sojka, "Modeling of coaxial powder flow for the laser direct deposition process," *Int. J. Heat Mass Transf.*, vol. 52, no. 25–26, pp. 5867–5877, Dec. 2009, doi: 10.1016/j.ijheatmasstransfer.2009.07.018.
[33] F. Mazzucato, S. Tusacciu, M. Lai, S. Biamino, M. Lombardi, and A. Valente, "Monitoring Approach to Evaluate the Performances of a New Deposition Nozzle Solution for DED Systems," *Technologies*, vol. 5, no. 2, p. 29, May 2017, doi: 10.3390/technologies5020029.
[34] X. Guan and Y. F. Zhao, "Numerical modeling of coaxial powder stream in laser-powder-based Directed Energy Deposition process," *Addit. Manuf.*, vol. 34, p. 101226, Aug. 2020, doi: 10.1016/j.addma.2020.101226.
[35] C. Katinas, W. Shang, Y. C. Shin, and J. Chen, "Modeling Particle Spray and Capture Efficiency for Direct Laser Deposition Using a Four Nozzle Powder Injection System," *J. Manuf. Sci. Eng.*, vol. 140, no. 4, p. 041014, Apr. 2018, doi: 10.1115/1.4038997.
[36] J. Montero, Á. Rodríguez, J. M. Amado, and A. J. Yáñez, "Inspection of Powder Flow During LMD Deposition by High Speed Imaging," *Phys. Procedia*, vol. 83, pp. 1319–1328, 2016, doi: 10.1016/j.phpro.2016.08.139.
[37] W. Devesse, D. De Baere, and P. Guillaume, "Modeling of laser beam and powder flow interaction in laser cladding using ray-tracing," *J. Laser Appl.*, vol. 27, no. S2, p. S29208, Feb. 2015, doi: 10.2351/1.4906394.
[38] S.-S. Jhang, Y.-L. Lo, and T.-N. Le, "Systematic modeling approach for analyzing the powder flow and powder energy absorptivity in direct energy deposition system," *Int. J. Adv. Manuf. Technol.*, vol. 105, no. 1–4, pp. 1765–1776, Nov. 2019, doi: 10.1007/s00170-019-04441-3.
[39] C. K. Kim, J. I. Jeong, S. G. Choi, J. H. Kim, and Y. T. Cho, "High-throughput directed energy deposition process with an optimized scanning nozzle," *J. Mater. Process. Technol.*, vol. 295, p. 117165, Sep. 2021, doi: 10.1016/j.jmatprotec.2021.117165.
[40] A. Martinez-Marchese, M. Ansari, M. Wang, A. Marzo, and E. Toyserkani, "On the application of sound radiation force for focusing of powder stream in directed energy deposition," *Ultrasonics*, vol. 127, p. 106830, Jan. 2023, doi: 10.1016/j.ultras.2022.106830.
[41] Z. Liu, H.-C. Zhang, S. Peng, H. Kim, D. Du, and W. Cong, "Analytical modeling and experimental validation of powder stream distribution during direct energy deposition," *Addit. Manuf.*, vol. 30, p. 100848, Dec. 2019, doi: 10.1016/j.addma.2019.100848.
[42] Y. Huang, M. B. Khamesee, and E. Toyserkani, "A comprehensive analytical model for laser powder-fed additive manufacturing," *Addit. Manuf.*, vol. 12, pp. 90–99, Oct. 2016, doi: 10.1016/j.addma.2016.07.001.
[43] S. J. Wolff *et al.*, "In-situ Observations of Directed Energy Deposition Additive Manufacturing Using High-Speed X-ray Imaging," *JOM*, vol. 73, no. 1, pp. 189–200, Jan. 2021, doi: 10.1007/s11837-020-04469-x.
[44] E. W. Reutzel and A. R. Nassar, "Laser DEDatabase and Process Development," Applied Research Laboratory, Pennsylvania State University, Technical Memorandum File No. 17-011, Aug. 2017.

[45] E. W. Reutzel and A. R. Nassar, “A survey of sensing and control systems for machine and process monitoring of directed-energy, metal-based additive manufacturing,” *Rapid Prototyp. J.*, vol. 21, no. 2, pp. 159–167, Mar. 2015, doi: 10.1108/RPJ-12-2014-0177.
[46] B. Thomas, “In-Situ Monitoring of Powder Flow in Directed Energy Deposition Additive Manufacturing,” The Pennsylvania State University, 2021.
[47] The MathWorks, Inc. (2022). MATLAB version: 9.10.0.1602886 (R2021a). Accessed: January 24, 2023. Available: https://www.mathworks.com.
[48] B. Bax, R. Rajput, R. Kellet, and M. Reisacher, “Systematic evaluation of process parameter maps for laser cladding and directed energy deposition,” *Addit. Manuf.*, vol. 21, pp. 487–494, May 2018, doi: 10.1016/j.addma.2018.04.002.